# Analysis Procedures for Evaluating Superheavy Load Movement on Flexible Pavements, Volume VII: Appendix F, Failure Analysis of Sloped Pavement Shoulders

PUBLICATION NO. FHWA-HRT-18-055

MARCH 2019

U.S. Department of Transportation
**Federal Highway Administration**

Research, Development, and Technology
Turner-Fairbank Highway Research Center
6300 Georgetown Pike
McLean, VA 22101-2296

## FOREWORD

The movement of superheavy loads (SHLs) on the Nation's highways is an increasingly common, vital economic necessity for many important industries, such as chemical, oil, electrical, and defense. Many superheavy components are extremely large and heavy (gross vehicle weights in excess of a few million pounds), and they often require specialized trailers and hauling units. At times, SHL vehicles have been assembled to suit the load being transported, and therefore, the axle configurations have not been standard or consistent. Accommodating SHL movements without undue damage to highway infrastructure requires the determination of whether the pavement is structurally adequate to sustain the SHL movement and protect any underground utilities. Such determination involves analysing the likelihood of instantaneous or rapid load-induced shear failure of the pavement structure.

The goal of this project was to develop a comprehensive analysis process for evaluating SHL movement on flexible pavements. As part of this project, a comprehensive mechanistic-based analysis approach consisting of several analysis procedures was developed for flexible pavement structures and documented in a 10-volume series of Federal Highway Administration reports—a final report and 9 appendices.[1–9] This is *Analysis Procedures for Evaluating Superheavy Load Movement on Flexible Pavements, Volume VII: Appendix F, Failure Analysis of Sloped Pavement Shoulders,* and it details the method developed for investigating the stability of sloped pavement shoulders under SHL-vehicle movements. It also presents verification of the proposed approach using the measurements obtained from tests on full-scale pavement structures. This report is intended for use by highway agency pavement engineers responsible for assessing the structural adequacy of pavements in the proposed route and identifying mitigation strategies, where warranted, in support of the agency's response to SHL-movement permit requests.

Cheryl Allen Richter, Ph.D., P.E.
Director, Office of Infrastructure
Research and Development

# TECHNICAL REPORT DOCUMENTATION PAGE

| | | |
|---|---|---|
| 1. Report No.<br>FHWA-HRT-18-055 | 2. Government Accession No. | 3. Recipient's Catalog No. |
| 4. Title and Subtitle<br>Analysis Procedures for Evaluating Superheavy Load Movement on Flexible Pavements, Volume VII: Appendix F, Failure Analysis of Sloped Pavement Shoulders | | 5. Report Date<br>March 2019<br>6. Performing Organization Code |
| 7. Author(s)<br>Hadi Nabizadeh (ORCID: 0000-0001-8215-1299), Raj V. Siddharthan (ORCID: 0000-0002-3847-7934), Sherif Elfass (ORCID: 0000-0003-3401-6513), and Elie Y. Hajj (ORCID: 0000-0001-8568-6360) | | 8. Performing Organization Report No.<br>WRSC-UNR-201710-01F |
| 9. Performing Organization Name and Address<br>Department of Civil and Environmental Engineering<br>University of Nevada<br>1664 North Virginia Street<br>Reno, NV 89557 | | 10. Work Unit No.<br>11. Contract or Grant No.<br>DTFH61-13-C-00014 |
| 12. Sponsoring Agency Name and Address<br>Office of Infrastructure Research and Development<br>Federal Highway Administration<br>Turner-Fairbank Highway Research Center<br>6300 Georgetown Pike<br>McLean, VA 22101 | | 13. Type of Report and Period Covered<br>Final Report; August 2013–July 2018<br>14. Sponsoring Agency Code<br>HRDI-20 |
| 15. Supplementary Notes<br>Nadarajah Sivaneswaran (HRDI-20; ORCID: 0000-0003-0287-664X), Office of Infrastructure Research and Development, Turner-Fairbank Highway Research Center, served as the Contracting Officer's Representative. | | |
| 16. Abstract<br>The movement of superheavy loads (SHLs) on the Nation's highways is an increasingly common, vital economic necessity for many important industries, such as chemical, oil, electrical, and defense. SHL hauling units are much larger in size and weight than standard trucks. SHL gross vehicle weights may be in excess of a few million pounds, so they often require specialized trailers and components with nonstandard spacing between tires and axles. Accommodating SHL-vehicle movements requires determining whether pavement is structurally adequate and analyzing the likelihood of instantaneous or rapid load-induced shear failure. As part of the Federal Highway Administration project, Analysis Procedures for Evaluating Superheavy Load Movement on Flexible Pavements, a method of investigating the stability of a sloped pavement shoulder under an SHL-vehicle movement was developed by modifying the well-accepted wedge method. This new method, with the use of 3D-Move Analysis software, is capable of considering a layered medium with distinct layer-stiffness values along with the unconventional SHL-vehicle loading configuration.(10) To account for the existence of a sloped pavement shoulder in 3D-Move Analysis, computed SHL vehicle-induced stresses are modified using a stress adjustment factor for a sloped shoulder ($SAF_{Shoulder}$). $SAF_{Shoulder}$ was determined based on results from large-scale pavement experiments conducted in this study. | | |
| 17. Key Words<br>Superheavy load, flexible pavement, large-scale testing, instrumentation, pavement shoulder, slope stability | 18. Distribution Statement<br>No restrictions. This document is available through the National Technical Information Service, Springfield, VA 22161.<br>http://www.ntis.gov | |

| 19. Security Classif. (of this report) | 20. Security Classif. (of this page) | 21. No. of Pages | 22. Price |
|---|---|---|---|
| Unclassified | Unclassified | 51 | N/A |

**Form DOT F 1700.7 (8-72)** Reproduction of completed page authorized.

# SI* (MODERN METRIC) CONVERSION FACTORS

## APPROXIMATE CONVERSIONS TO SI UNITS

| Symbol | When You Know | Multiply By | To Find | Symbol |
|---|---|---|---|---|
| | | **LENGTH** | | |
| in | inches | 25.4 | millimeters | mm |
| ft | feet | 0.305 | meters | m |
| yd | yards | 0.914 | meters | m |
| mi | miles | 1.61 | kilometers | km |
| | | **AREA** | | |
| $in^2$ | square inches | 645.2 | square millimeters | $mm^2$ |
| $ft^2$ | square feet | 0.093 | square meters | $m^2$ |
| $yd^2$ | square yard | 0.836 | square meters | $m^2$ |
| ac | acres | 0.405 | hectares | ha |
| $mi^2$ | square miles | 2.59 | square kilometers | $km^2$ |
| | | **VOLUME** | | |
| fl oz | fluid ounces | 29.57 | milliliters | mL |
| gal | gallons | 3.785 | liters | L |
| $ft^3$ | cubic feet | 0.028 | cubic meters | $m^3$ |
| $yd^3$ | cubic yards | 0.765 | cubic meters | $m^3$ |
| | | NOTE: volumes greater than 1000 L shall be shown in $m^3$ | | |
| | | **MASS** | | |
| oz | ounces | 28.35 | grams | g |
| lb | pounds | 0.454 | kilograms | kg |
| T | short tons (2000 lb) | 0.907 | megagrams (or "metric ton") | Mg (or "t") |
| | | **TEMPERATURE (exact degrees)** | | |
| $^oF$ | Fahrenheit | 5 (F-32)/9<br>or (F-32)/1.8 | Celsius | $^oC$ |
| | | **ILLUMINATION** | | |
| fc | foot-candles | 10.76 | lux | lx |
| fl | foot-Lamberts | 3.426 | candela/$m^2$ | $cd/m^2$ |
| | | **FORCE and PRESSURE or STRESS** | | |
| lbf | poundforce | 4.45 | newtons | N |
| $lbf/in^2$ | poundforce per square inch | 6.89 | kilopascals | kPa |

## APPROXIMATE CONVERSIONS FROM SI UNITS

| Symbol | When You Know | Multiply By | To Find | Symbol |
|---|---|---|---|---|
| | | **LENGTH** | | |
| mm | millimeters | 0.039 | inches | in |
| m | meters | 3.28 | feet | ft |
| m | meters | 1.09 | yards | yd |
| km | kilometers | 0.621 | miles | mi |
| | | **AREA** | | |
| $mm^2$ | square millimeters | 0.0016 | square inches | $in^2$ |
| $m^2$ | square meters | 10.764 | square feet | $ft^2$ |
| $m^2$ | square meters | 1.195 | square yards | $yd^2$ |
| ha | hectares | 2.47 | acres | ac |
| $km^2$ | square kilometers | 0.386 | square miles | $mi^2$ |
| | | **VOLUME** | | |
| mL | milliliters | 0.034 | fluid ounces | fl oz |
| L | liters | 0.264 | gallons | gal |
| $m^3$ | cubic meters | 35.314 | cubic feet | $ft^3$ |
| $m^3$ | cubic meters | 1.307 | cubic yards | $yd^3$ |
| | | **MASS** | | |
| g | grams | 0.035 | ounces | oz |
| kg | kilograms | 2.202 | pounds | lb |
| Mg (or "t") | megagrams (or "metric ton") | 1.103 | short tons (2000 lb) | T |
| | | **TEMPERATURE (exact degrees)** | | |
| $^oC$ | Celsius | 1.8C+32 | Fahrenheit | $^oF$ |
| | | **ILLUMINATION** | | |
| lx | lux | 0.0929 | foot-candles | fc |
| $cd/m^2$ | candela/$m^2$ | 0.2919 | foot-Lamberts | fl |
| | | **FORCE and PRESSURE or STRESS** | | |
| N | newtons | 0.225 | poundforce | lbf |
| kPa | kilopascals | 0.145 | poundforce per square inch | $lbf/in^2$ |

## ANALYSIS PROCEDURES FOR EVALUATING SUPERHEAVY LOAD MOVEMENT ON FLEXIBLE PAVEMENTS PROJECT REPORT SERIES

This volume is the seventh of 10 volumes in this research report series. Volume I is the final report, and Volume II through Volume X consist of Appendix A through Appendix I. Any reference to a volume in this series will be referenced in the text as "Volume II: Appendix A," "Volume III: Appendix B," and so forth. The following list contains the volumes:

| Volume | Title | Report Number |
|---|---|---|
| I | Analysis Procedures for Evaluating Superheavy Load Movement on Flexible Pavements, Volume I: Final Report | FHWA-HRT-18-049 |
| II | Analysis Procedures for Evaluating Superheavy Load Movement on Flexible Pavements, Volume II: Appendix A, Experimental Program | FHWA-HRT-18-050 |
| III | Analysis Procedures for Evaluating Superheavy Load Movement on Flexible Pavements, Volume III: Appendix B, Superheavy Load Configurations and Nucleus of Analysis Vehicle | FHWA-HRT-18-051 |
| IV | Analysis Procedures for Evaluating Superheavy Load Movement on Flexible Pavements, Volume IV: Appendix C, Material Characterization for Superheavy Load Movement Analysis | FHWA-HRT-18-052 |
| V | Analysis Procedures for Evaluating Superheavy Load Movement on Flexible Pavements, Volume V: Appendix D, Estimation of Subgrade Shear Strength Parameters Using Falling Weight Deflectometer | FHWA-HRT-18-053 |
| VI | Analysis Procedures for Evaluating Superheavy Load Movement on Flexible Pavements, Volume VI: Appendix E, Ultimate and Service Limit Analyses | FHWA-HRT-18-054 |
| VII | Analysis Procedures for Evaluating Superheavy Load Movement on Flexible Pavements, Volume VII: Appendix F, Failure Analysis of Sloped Pavement Shoulders | FHWA-HRT-18-055 |
| VIII | Analysis Procedures for Evaluating Superheavy Load Movement on Flexible Pavements, Volume VIII: Appendix G, Risk Analysis of Buried Utilities Under Superheavy Load Vehicle Movements | FHWA-HRT-18-056 |
| IX | Analysis Procedures for Evaluating Superheavy Load Movement on Flexible Pavements, Volume IX: Appendix H, Analysis of Cost Allocation Associated with Pavement Damage Under a Superheavy Load Vehicle Movement | FHWA-HRT-18-057 |
| X | Analysis Procedures for Evaluating Superheavy Load Movement on Flexible Pavements, Volume X: Appendix I, Analysis Package for Superheavy Load Vehicle Movement on Flexible Pavement (SuperPACK) | FHWA-HRT-18-058 |

## TABLE OF CONTENTS

## LIST OF FIGURES

## LIST OF TABLES

## LIST OF ABREVIATIONS AND SYMBOLS

### Abbreviations

| | |
|---|---|
| 3D | three-dimensional |
| AC | asphalt concrete |
| CAB | crushed aggregate base |
| FWD | falling weight deflectometer |
| Loc | location |
| No. | number |
| SG | subgrade |
| SHL | superheavy load |
| TEPC | total earth pressure cell |

### Symbols

| | |
|---|---|
| $A_{SG}$ | trapezoidal side surfaces composed of subgrade |
| $B_{wedge}$ | width of the wedge |
| $c$ | cohesion |
| $c_D$ | developed cohesion |
| $F_D$ | resultant force from the bottom soil (slip surface) |
| $FOS$ | factor of safety |
| $K_a$ | Rankine active earth pressure coefficient |
| $K_p$ | Rankine passive earth pressure coefficient |
| $l$ | length of bottom slip surface |
| $P$ | resultant horizontal force due to a surcharge load |
| $P_D$ | resistive force from the side soil that makes an angle the resultant force makes with the normal to the bottom slip surface with the normal to the side surfaces (i.e., front and back) |
| $Q$ | lateral earth pressure from the adjacent soil |
| $SAF_{Shoulder}$ | stress adjustment factor for a sloped shoulder |
| $T'_D$ | developed resisting cohesion force resulting from mobilized cohesion acting on the side surfaces (i.e., front and back) |
| $T_D$ | mobilized cohesion acting on the bottom slip surface |
| $W$ | weight of the sliding wedge |
| $\theta_{wedge}$ | angle between the slip surface and horizontal surface |
| $\sigma_0$ | vertical soil pressure |
| $\sigma_a$ | Rankine active earth pressure |
| $\sigma_n$ | normal stress on the failure plane |
| $\sigma_P$ | Rankine passive earth pressure |
| $\sigma_v$ | vertical stress |
| $\tau_{induced}$ | induced shear stress |
| $\tau_{strength}$ | shear strength |
| $\phi$ | angle of internal friction |
| $\phi_D$ | developed angle of internal friction |

# CHAPTER 1. INTRODUCTION

Many industries, such as chemical, oil, electrical, and defense, require the movement of superheavy loads (SHLs) on the Nation's highways. SHL hauling units are much larger in size and weight than standard trucks, often with gross vehicle weights in excess of a few million pounds. Accordingly, SHL vehicles frequently necessitates specialized trailers and components with nonstandard spacing between tires and axles. Accommodating SHL-vehicle movements requires determining whether pavement is structurally adequate and analyzing the likelihood of instantaneous or rapid load-induced shear failure. Figure 1 shows the flowchart of the overall approach developed as part of this Federal Highway Administration project, Analysis Procedures for Evaluating Superheavy Load Movement on Flexible Pavements. In general, the approach consists of the following four major components:

- Ultimate failure analyses.
- Buried utility risk analysis.
- Service limit analyses.
- Cost allocation analysis.

Mitigation strategies may be needed at any stage of the evaluation process when the calculated results fail to meet the respective requirements imposed (e.g., when results indicate a high potential for shear failure of the pavement or damage to buried utilities).

As shown in figure 1, the first step of this approach involves a risk analysis of instantaneous or rapid load-induced ultimate shear failure. Subgrade (SG) is generally the weakest layer in a pavement structure. Thus, a bearing failure analysis should be performed to investigate the likelihood of general bearing capacity failure under an SHL vehicle within the influenced zone of an SG layer. Sloped-shoulder failure analysis, which examines the bearing capacity failure and edge-slope stability associated with a sloped ground under an SHL-vehicle movement, would be the next step. If the ultimate failure analyses reveal no failure in the sloped shoulder, a buried utility risk analysis should be conducted (when applicable). In this analysis, induced stresses and deflections by an SHL vehicle on existing buried utilities are evaluated and compared to established design criteria. Subsequently, if no mitigation strategies are needed, service limit analyses for localized shear failure and deflection-based service limits should be conducted. A localized shear failure analysis is performed to investigate the possibility of failure at the critical location on top of an SG layer under an SHL vehicle. A deflection-based service limit analysis assesses the magnitude of load-induced pavement deflections during an SHL-vehicle movement. This analysis, for instance, may suggest the need for mitigation strategies to meet the imposed acceptable surface-deflection limits. After successfully completing all previously described analyses (i.e., ultimate failure analyses, buried utility risk analysis, and service limit analyses), a cost allocation analysis should be conducted.

A summary of the various analysis procedures developed in this study and the associated objectives (including related volume numbers) are summarized in table 1. This report (Volume VII: Appendix F) is the seventh of 10 volumes and presents the slope-stability approach that allows for the stability analysis of a sloped shoulder subjected to an SHL-vehicle movement.

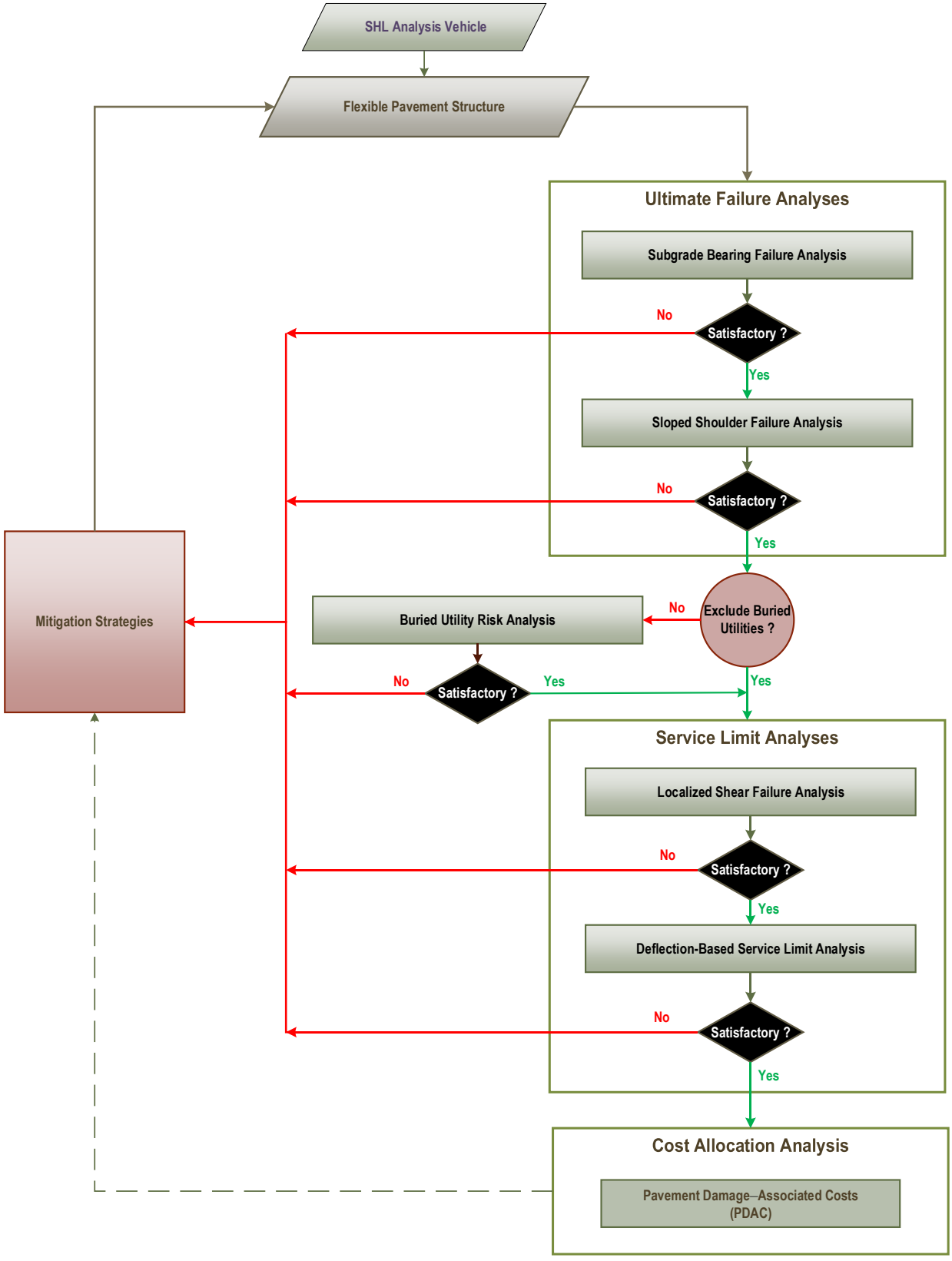




**Figure 1. Flowchart. Overall SHL-vehicle analysis methodology.**

**Table 1. Developed analysis procedures to evaluate SHL movement on flexible pavements.**

| Procedure | Objective |
|---|---|
| SHL analysis vehicle | Identify segment(s) of the SHL vehicle configuration that can be regarded as representative of the entire SHL vehicle (Volume III: Appendix B)[3] |
| Flexible pavement structure | Characterize representative material properties for existing pavement layers (Volume IV: Appendix C and Volume V: Appendix D)[4] |
| SG bearing failure analysis | Investigate instantaneous ultimate shear failure in pavement SG (Volume VI: Appendix E)[6] |
| Sloped-shoulder failure analysis | Examine the stability of sloped pavement shoulders under SHL-vehicle movement (Volume VII: Appendix F) |
| Buried utility risk analysis | Perform risk analysis of existing buried utilities (Volume VIII: Appendix G)[7] |
| Localized shear failure analysis | Inspect the likelihood of localized failure (yield) in the pavement SG (Volume VI: Appendix E)[6] |
| Deflection-based service limit analysis | Investigate the development of premature surface distresses (Volume VI: Appendix E)[6] |
| Cost allocation analysis | Determine pavement damage–associated cost attributable to SHL-vehicle movement (Volume IX: Appendix H)[8] |

SHL vehicles are usually moved during periods of controlled traffic, so it is often possible to keep SHL vehicles far from the edges and shoulders of a pavement. Due to narrow lanes or wide SHL vehicles, however, keeping SHL vehicles away from a pavement edge, particularly on routes where there is an unpaved shoulder and/or a steep slope, is not always possible. Therefore, it is necessary to investigate the stability of sloped pavement shoulders under SHL-vehicle movements.

Although slope stability is a common problem in geotechnical practice, it has not been a major concern for roads subjected to only standard truck loading. However, substantially higher surcharge loads resulting from SHL-vehicle movements might lead to sloped shoulder failure. Fernando hypothesized that the role of an SHL vehicle can be investigated by comparing pavement responses at the edges and interior of a lane under falling weight deflectometer (FWD) loading.[11] However, analysis of the stability of a sloped shoulder under SHL-vehicle movements had not been undertaken. Such an analysis requires information, including geometry, failure planes, and shear strength ($\tau_{strength}$) parameters.

In this study, the wedge method, which is a common means of analyzing slope stability in geotechnical practices, was modified to evaluate the stability of a sloped, layered medium consisting of typical pavement-layer configurations and properties subjected to an SHL-vehicle movement.

In geotechnical practice, the Boussinesq theory, which is limited to a homogenous soil medium, is routinely used to determine stress distribution. In this study, 3D-Move Analysis software was

used to compute stress distributions within the layered medium of a pavement.[10] 3D-Move Analysis was considered an ideal candidate for stress distributions computation because it can account for viscoelastic properties of an asphalt concrete (AC) layer as well as for a moving load with nonuniform tire–pavement interface stresses on a loaded area of any shape. However, this software assumes that pavement layers extend laterally to infinity. Therefore, the role of a sloped shoulder on stress distributions near the edge of a pavement should be accounted for when this software is used to compute SHL vehicle–induced stresses on a shoulder. To address this issue, the stresses computed using 3D-Move Analysis are modified using a stress adjustment factor for a sloped shoulder ($SAF_{Shoulder}$). In this report, $SAF_{Shoulder}$, determined based on large-scale experiments (i.e., experiment number (No.) 3 and experiment No. 4), is presented. The validation of the proposed methodology is also presented and discussed.

## CHAPTER 2. SLOPE STABILITY–ANALYSIS METHODOLOGY

Conventional slope-stability approaches are based on a limit equilibrium analysis of a mass of soil bounded between an assumed possible slip surface(s) and slope surface. Failure is investigated by comparing the corresponding driving and resisting sliding forces and moments. Such approaches are generally categorized as limit equilibrium analyses, and to identify the most critical slip surface, they consider several of these surfaces for possible failure. In general, the stability of a soil mass depends upon its weight, the external forces acting upon it (such as surcharges), and $\tau_{strength}$ and porewater pressures along the slip surface(s). The stability of a slope is investigated by calculating a factor of safety (*FOS*), which is defined as the ratio of the available $\tau_{strength}$ to the induced shear stress ($\tau_{induced}$) required for equilibrium. In an analysis based on total stresses, the *FOS* is evaluated using the equations shown in figure 2 and figure 3.

$$FOS = \frac{\tau_{strength}}{\tau_{induced}}$$

**Figure 2. Equation. Calculation of *FOS* for slope-stability analysis.**

$$\tau_{strength} = c + \sigma_n \tan\phi$$

**Figure 3. Equation. Calculation of $\tau_{strength}$.**

Where:

$c$ = cohesion.
$\phi$ = angle of internal friction.
$\sigma_n$ = normal stress on the failure plane.

By rewriting the equation in figure 2, the allowable $\tau_{induced}$ to maintain stability can be expressed by the equation in figure 4. The terms on the right-hand side of the equation in figure 4 represent the developed (i.e., mobilized) $c$ ($c_D$) (figure 5) and developed $\phi$ ($\phi_D$) (figure 6), respectively.

$$\tau_{induced} = \frac{c}{FOS} + \frac{\sigma_n \tan\phi}{FOS}$$

**Figure 4. Equation. Allowable $\tau_{induced}$ required for equilibrium.**

$$c_D = \frac{c}{FOS}$$

**Figure 5. Equation. Calculation of $c_D$.**

$$\tan\phi_D = \frac{\tan\phi}{FOS}$$

**Figure 6. Equation. Calculation of $\tan\phi_D$.**

By assuming a value for *FOS* and calculating the corresponding mobilized shear stress, a possible static equilibrium condition between resisting and driving forces and moments can be determined. This process is repeated until the minimum value of *FOS* is determined.

Many limit equilibrium methods, such as the ordinary method of slices, simplified Bishop, modified Swedish method, and Spencer's method, use different assumptions to achieve a solution because the slope-stability problem is statically indeterminate. Methods, such as the Morgenstern–Price method, that satisfy all static equilibrium conditions are referred to as "complete" equilibrium methods. Although complete equilibrium methods are generally more accurate than "incomplete" ones (e.g., simplified Bishop method), they do require a rigorous and time-consuming analysis. However, incomplete equilibrium methods are often sufficiently accurate and have been useful for many practical applications (e.g., water retaining structures and tailings dams).[12,13] All such methods assume a plane strain condition, and therefore, only vertical cross sections are used in the analysis.

## 2.1. WEDGE METHOD

The wedge method has been used extensively by the U.S. Army Corps of Engineers and the geotechnical engineering community for slope-stability analysis.[12,13] This method satisfies the force equilibrium in both horizontal and vertical directions but does not satisfy the moment equilibrium. The use of circular failure surfaces is appropriate for homogeneous slopes; for layered soils, however, especially when layers with contrasting strength characteristics are present in the domain, the wedge method has been recommended by U.S. Army Corps of Engineers.[12] The wedge method is appropriate for investigating the stability of a sloped shoulder subjected to an SHL-vehicle movement, but it needs to be modified when a layered medium exists. This chapter summarizes the modified wedge method developed in this study.

Figure 7 illustrates a typical flexible pavement structure with a sloped shoulder. As illustrated in this figure, to investigate the stability of a pavement shoulder subjected to an SHL-vehicle movement, various wedges of failure are selected. This figure shows several slip surfaces passing through point A as solid lines. In all cases, the failure wedge is bounded by a vertical plane, and a horizontal or inclined slip surface is located in the SG layer. The vertical plane is located to the left of the AC layer as it is assumed that the vertical plane cannot extend through the AC layer. It is also assumed that the slip surface is developed in the SG layer because it is the weakest layer in the pavement structure. Searching for the critical location of the failure wedge involves systematically varying the horizontal boundaries of the wedges until the corresponding minimum *FOS* is found.

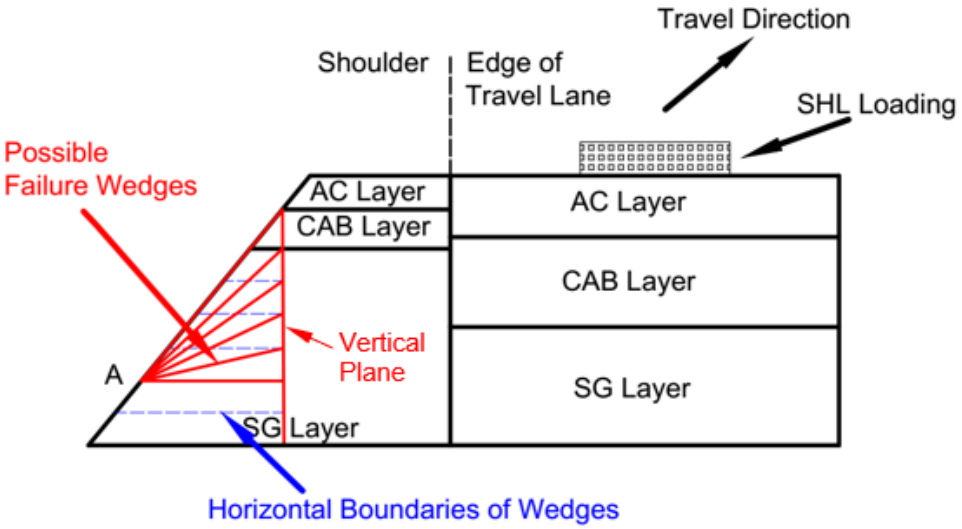



CAB = crushed aggregate base.

**Figure 7. Illustration. Search schemes for failure wedges.**

The stability of each failure wedge is evaluated by considering the wedge as a rigid sliding mass or a gravity-retaining structure. As shown in figure 8 and figure 9, five forces acting on the failure wedge can be identified as follows:

- The weight of the sliding wedge ($W$).
- The developed resisting $c$ force resulting from the mobilized $c$ acting on the bottom slip surface ($T_D$).
- The resultant force from the bottom soil (slip surface) ($F_D$) that makes $\phi_D$.
- The two components of horizontal driving forces acting on the vertical plane: lateral earth pressure from the adjacent soil ($Q$) and resultant horizontal force due to a surcharge load ($P$) (i.e., SHL vehicle).

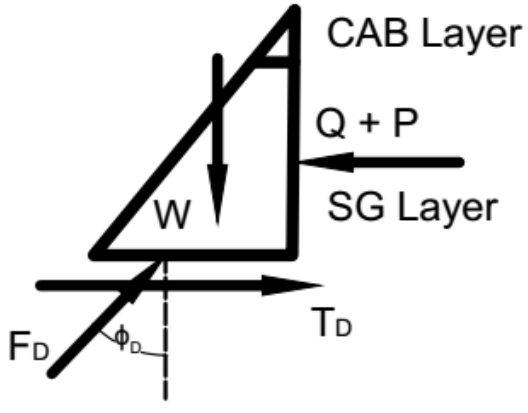



CAB = crushed aggregate base.

**Figure 8. Illustration. Failure wedge with horizontal slip surface and applied forces.**

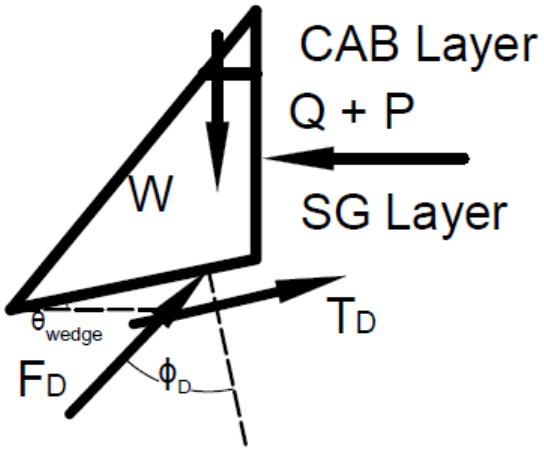



CAB = crushed aggregate base.

**Figure 9. Illustration. Failure wedge with inclined slip surface and applied forces.**

To determine *FOS*, the force equilibrium equations in parallel and perpendicular directions to the slip surface are applied. Consequently, *FOS* using the equation presented in figure 10 or figure 11 can be determined. Here, $\theta_{wedge}$ is the angle between the slip surface and horizontal surface (figure 9), and *l* is the length of the bottom slip surface. For the failure wedges with a horizontal slip surface where $\theta_{wedge}$ is 0, *FOS* can be simplified to the equation shown in figure 11. To investigate the stability of a sloped shoulder under an SHL-vehicle movement, the slope stability–analysis module, which is capable of analyzing all possible failure wedges, was incorporated into the Superheavy Load Pavement Analysis PACKage (SuperPACK).

$$FOS = \frac{(W\cos\theta_{wedge} - (Q+P)\sin\theta_{wedge})\tan\phi + cl}{(W\sin\theta_{wedge} + (Q+P)\cos\theta_{wedge})}$$

**Figure 10. Equation. *FOS* against failure for wedges with an inclined slip surface.**

$$FOS = \frac{W\tan\phi + cl}{P+Q}$$

**Figure 11. Equation. *FOS* against failure for wedges with a horizontal slip surface.**

*Q* is calculated by using Rankine active earth pressure ($\sigma_a$), which is a well-accepted procedure for designing retaining structures.[14] This is achieved by integrating the distribution of $\sigma_a$ along the vertical plane of the failure wedge under consideration. $\sigma_a$ is calculated using figure 12 as a function of the vertical soil pressure ($\sigma_0$), *c*, and the Rankine active pressure coefficient ($K_a$) that is defined in figure 13.

$$K_a = \tan^2\left(45 - \frac{\phi}{2}\right)$$

**Figure 12. Equation. Calculation of $K_a$.**

$$\sigma_a = \sigma_0 K_a - 2c\sqrt{K_a}$$

**Figure 13. Equation. Calculation of $\sigma_a$.**

*P* is calculated by using the load-induced horizontal stress distribution on the sliding wedge based on the Boussinesq theory.(14) This means that an elastic, homogenous, and isotropic semi-infinite soil medium is assumed. Subsequently, the load-induced horizontal stress on the sliding wedge calculated using the Boussinesq theory is doubled to account for the yielding soil continuum. In other words, the stresses given by the Boussinesq solution are multiplied by $SAF_{Shoulder}$ with a value equal to 2. It should be noted that *P* is the integration of the calculated load-induced horizontal stress distribution along the vertical plane of the same failure wedge under consideration.

These assumptions may not hold true for a pavement structure with layers that have distinct strength properties. Moreover, the complex loading configuration of an SHL vehicle cannot be handled by Boussinesq equations. Since 3D-Move Analysis can account for the viscoelastic properties of an AC layer, nonuniform tire–pavement interface stresses on a loaded area of any shape, as well as moving loads, it was an ideal candidate for computing load-induced horizontal stresses of sloped shoulders. However, computed lateral stresses using 3D-Move Analysis, which assumes the pavement layers extend laterally to infinity, are a concern. To address this issue, a modification of 3D-Move Analysis computed stresses using $SAF_{Shoulder}$ was proposed. Discussion regarding the determination of $SAF_{Shoulder}$ is presented in the next chapter.

# CHAPTER 3. DETERMINATION OF $SAF_{Shoulder}$

To determine a suitable $SAF_{Shoulder}$ for sloped shoulder stability analysis, large-scale tests of a sloped edge (i.e., experiment No. 4) were conducted. A careful comparison between experiment No. 3 (which had no sloped pavement shoulder) and experiment No. 4 identified the role of a sloped edge in the stress distribution within a typical pavement structure. This chapter first describes both experiments along with corresponding observations and then describes the exercise to determine $SAF_{Shoulder}$.

## 3.1. DESCRIPTION OF LARGE-SCALE EXPERIMENTS

As the main objective of this comparative analysis was to determine the role of a sloped shoulder in the load-carrying capacity of a pavement structure under an SHL-vehicle movement, the same pavement structure, materials, and construction practice were used in experiment No. 3 and experiment No. 4.

Experiment No. 3 included FWD testing on the full pavement structure, which was composed of 5 inches of AC, 6 inches of crushed aggregate base (CAB), and 66 inches of SG. FWD loads of 9,000; 12,000; 16,000; 21,000; and 27,000 lb were applied to the pavement surface and in the middle of the pavement. Figure 14 through figure 17 detail the instrumentation plans. A detailed discussion regarding the large-scale experiments (construction practice, instrumentation, material properties, etc.) can be found in Volume II: Appendix A.[2]

In experiment No. 4, a full pavement structure was constructed with a total thickness of 77 inches and a side slope of 1:1.5 (33.7 degrees with the horizontal). Figure 18 through figure 24 are drawings of the experiment setup. Similar to experiment No. 3, the pavement structure consisted of 5 inches of AC, 6 inches of CAB, and 66 inches of SG. FWD loads were applied on top of the AC layer at the following three locations: 12, 24, and 36 inches from the edge of the pavement (i.e., the slope). Similar to experiment No. 3, FWD loads of 9,000; 12,000; 16,000; 21,000; and 27,000 lb were applied at each of three locations. These locations are referred to as Loc12, Loc24, and Loc36, respectively.

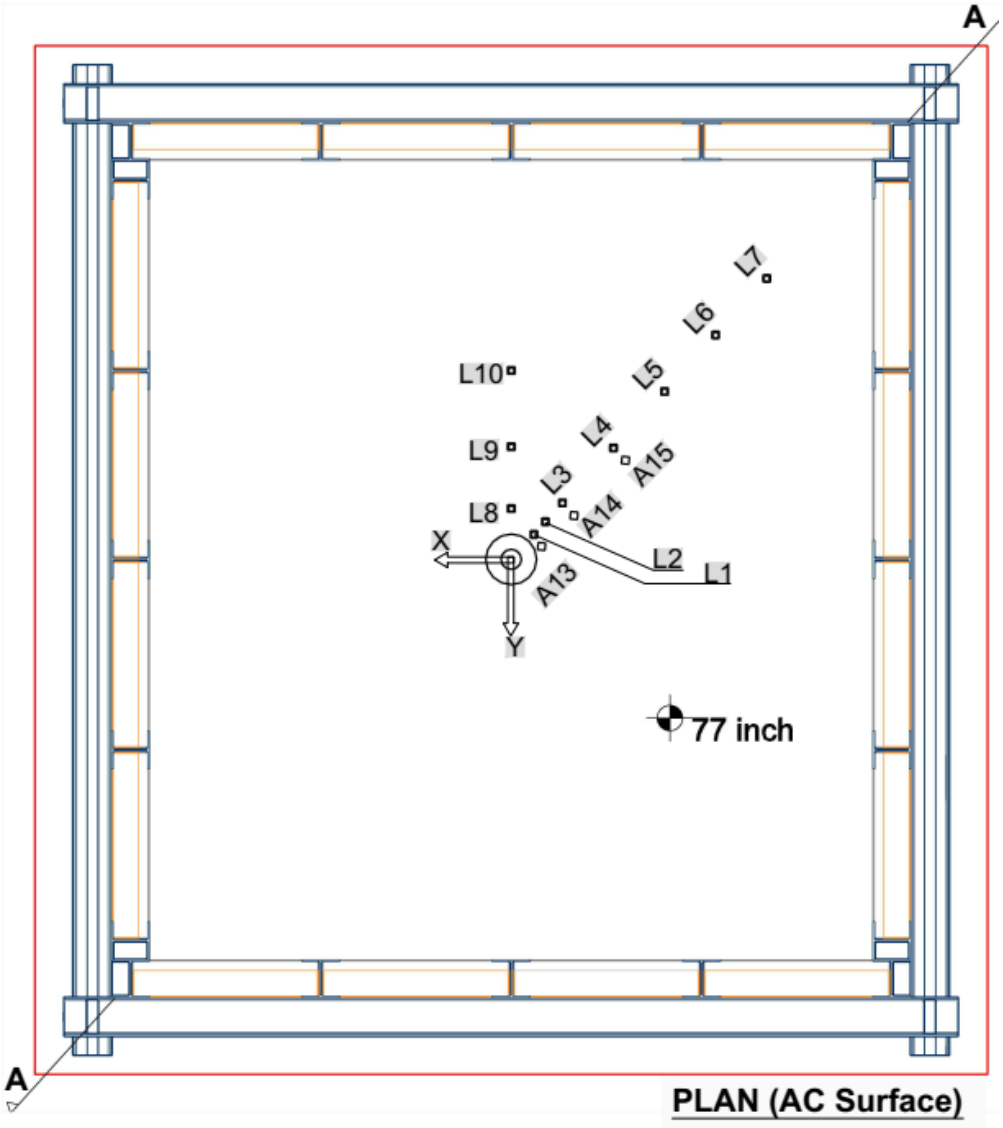



L = linear variable differential transformer; A = accelerometer.

**Figure 14. Illustration. Plan view for large-scale-box instrumentations in experiment No. 3.**

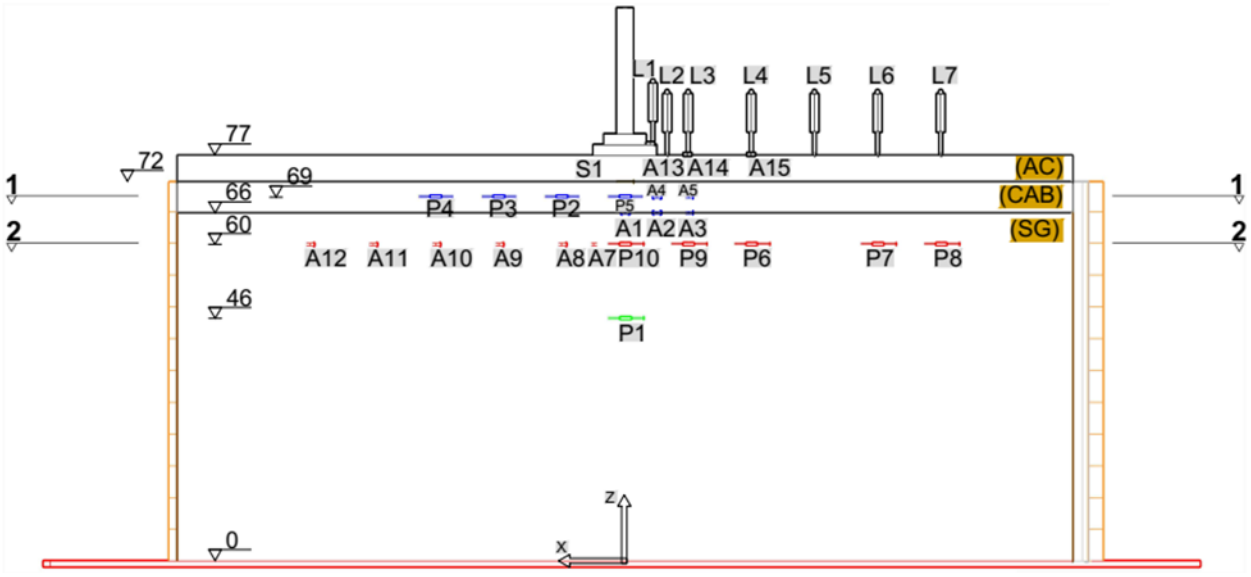



Note: All elevations are in inches.
L = linear variable differential transformer; P = total earth pressure cell; A = accelerometer.

**Figure 15. Illustration. Section A-A view for large-scale-box instrumentations in experiment No. 3.**

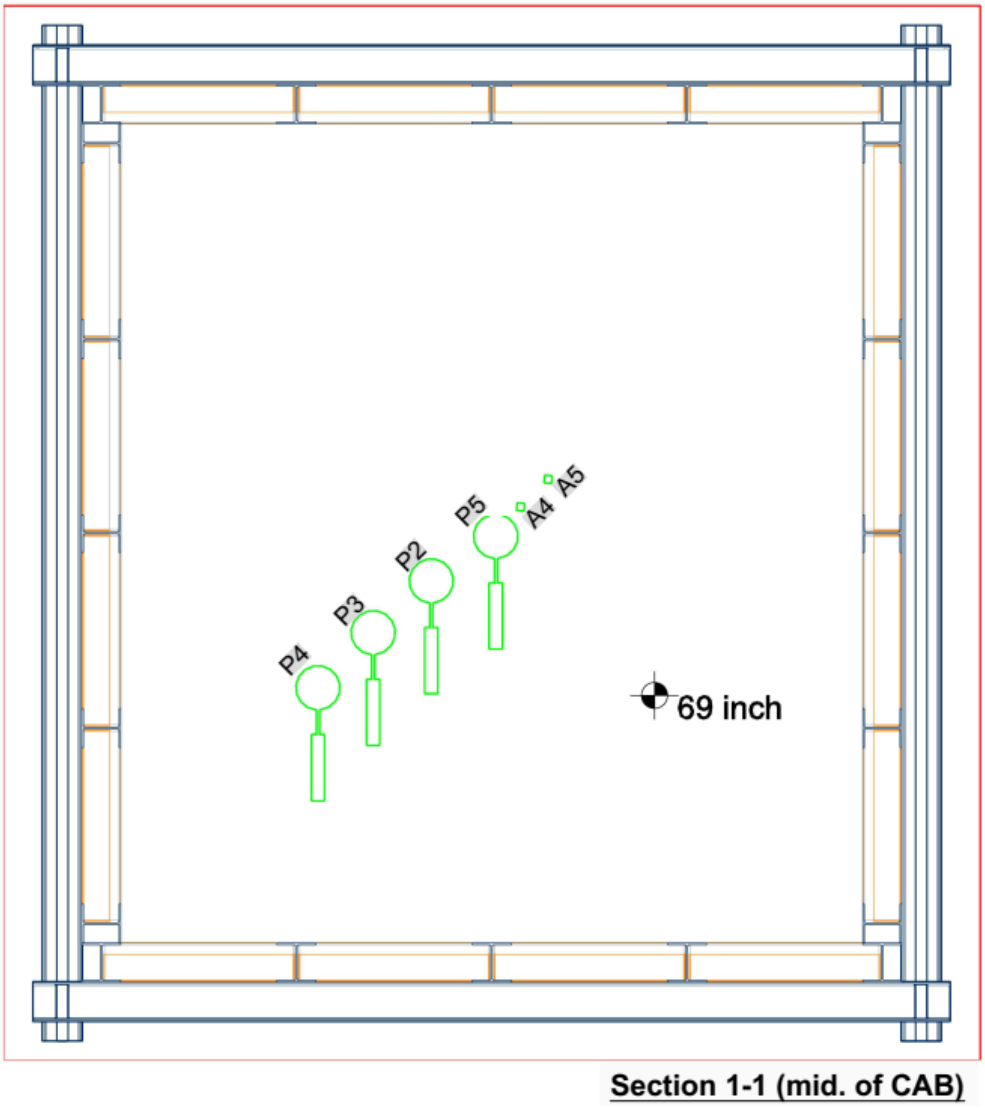



P = total earth pressure cell; A = accelerometer.

**Figure 16. Illustration. Section 1-1 view for large-scale-box instrumentations in experiment No. 3.**

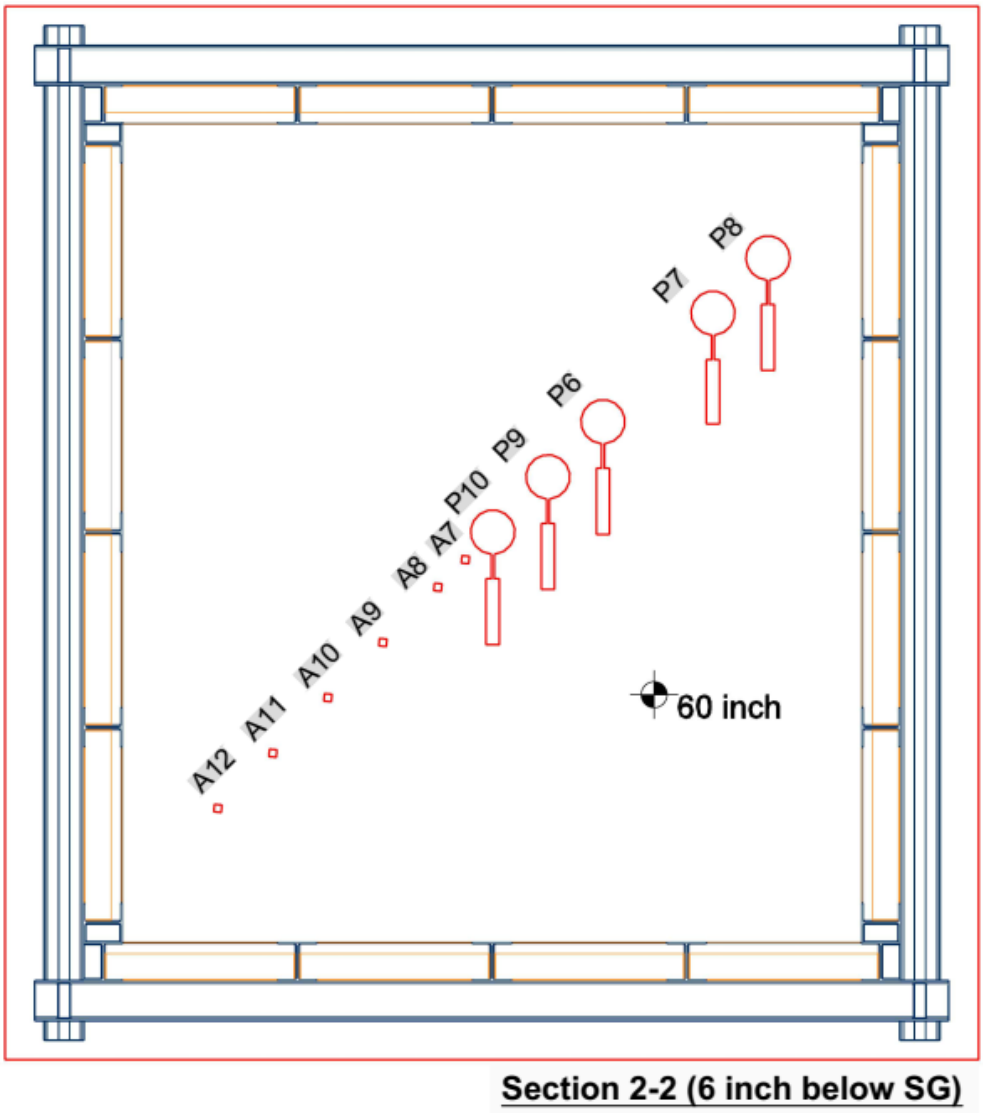



P = total earth pressure cell; A = accelerometer.

**Figure 17. Illustration. Section 2-2 view for large-scale-box instrumentations in experiment No. 3.**

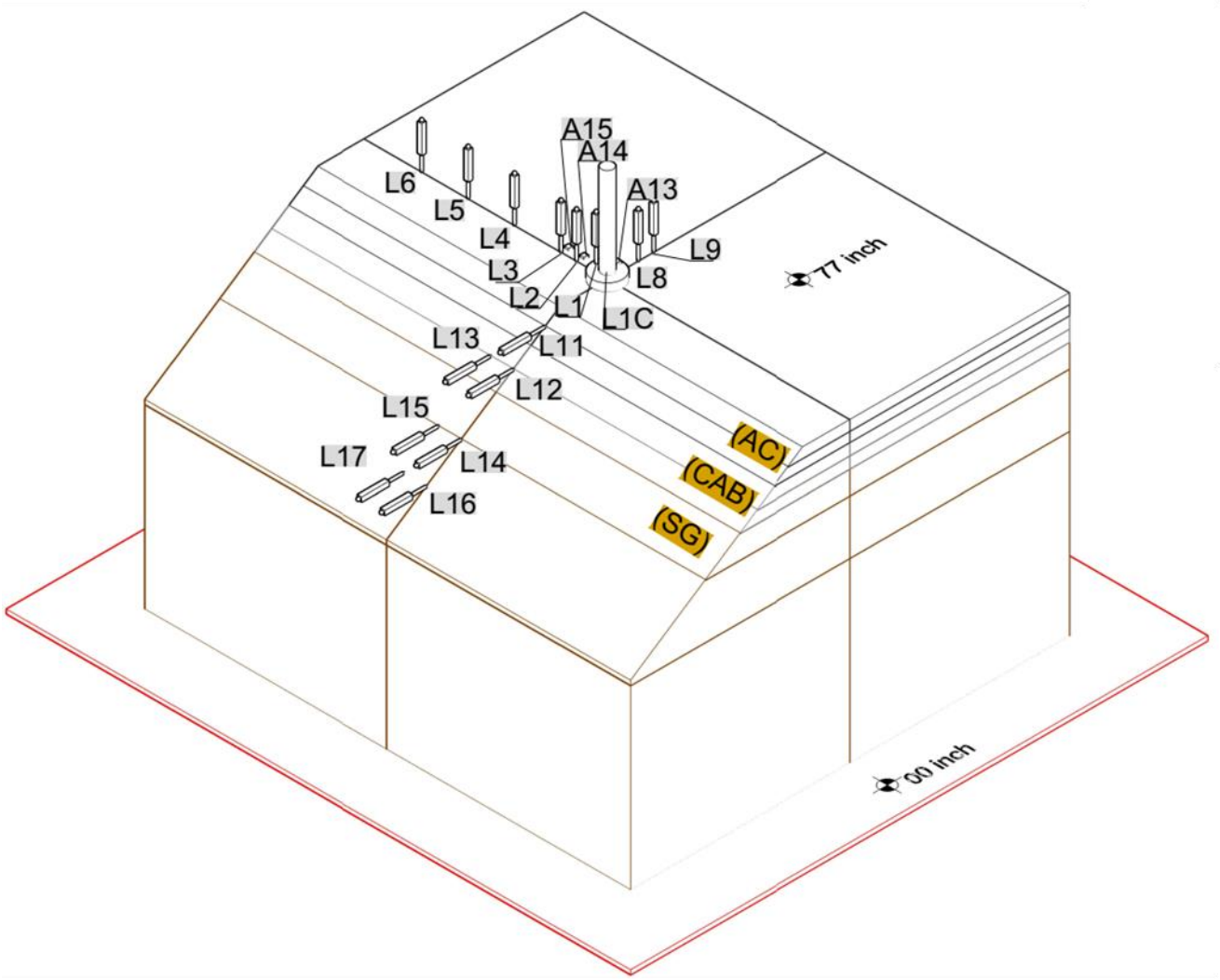



L = linear variable differential transformer; A = accelerometer.

**Figure 18. Illustration. 3D view of large-scale-box instrumentations in experiment No. 4 (elevation of 77 inches).**

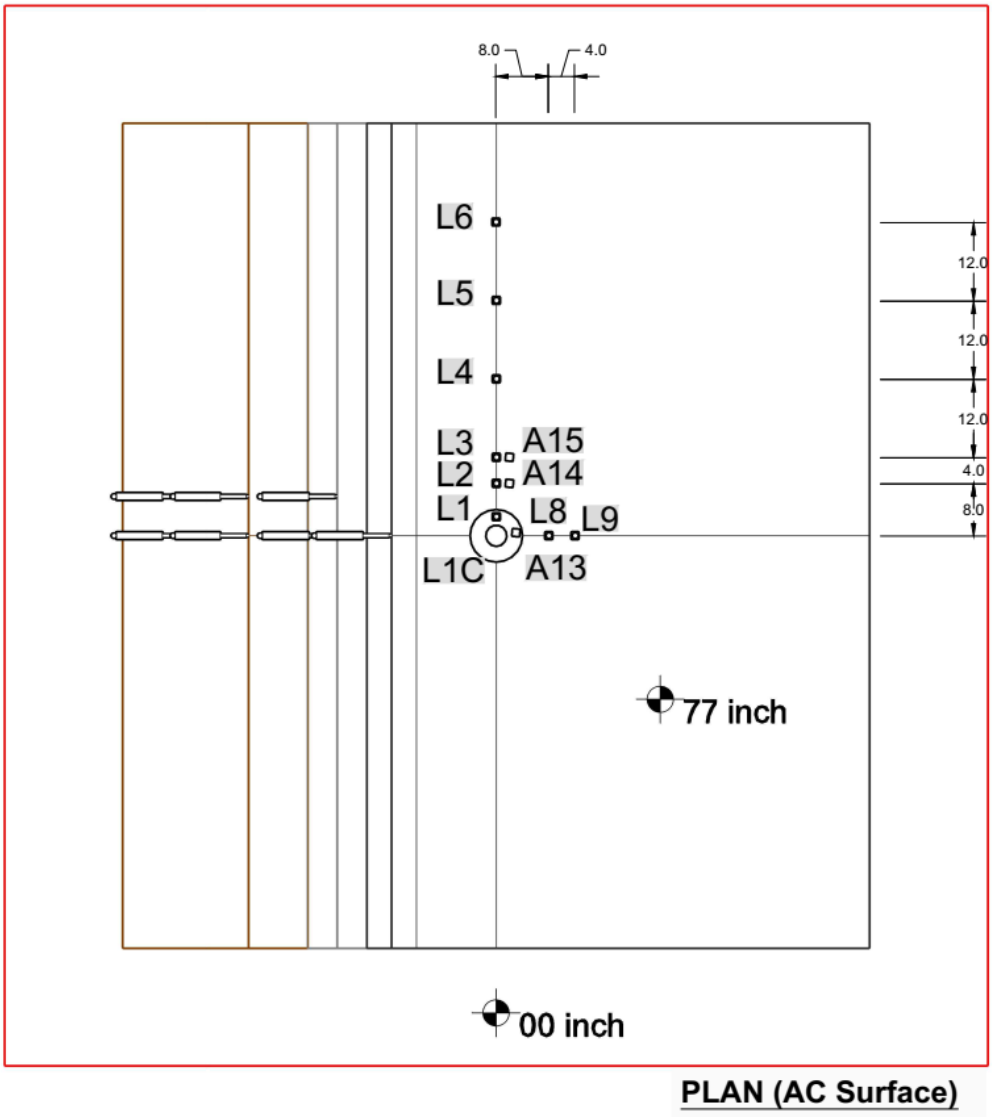



Note: All dimensions are in inches.
L = linear variable differential transformer; A = accelerometer.

**Figure 19. Illustration. Plan view for large-scale-box instrumentations in experiment No. 4 (elevation of 77 inches).**

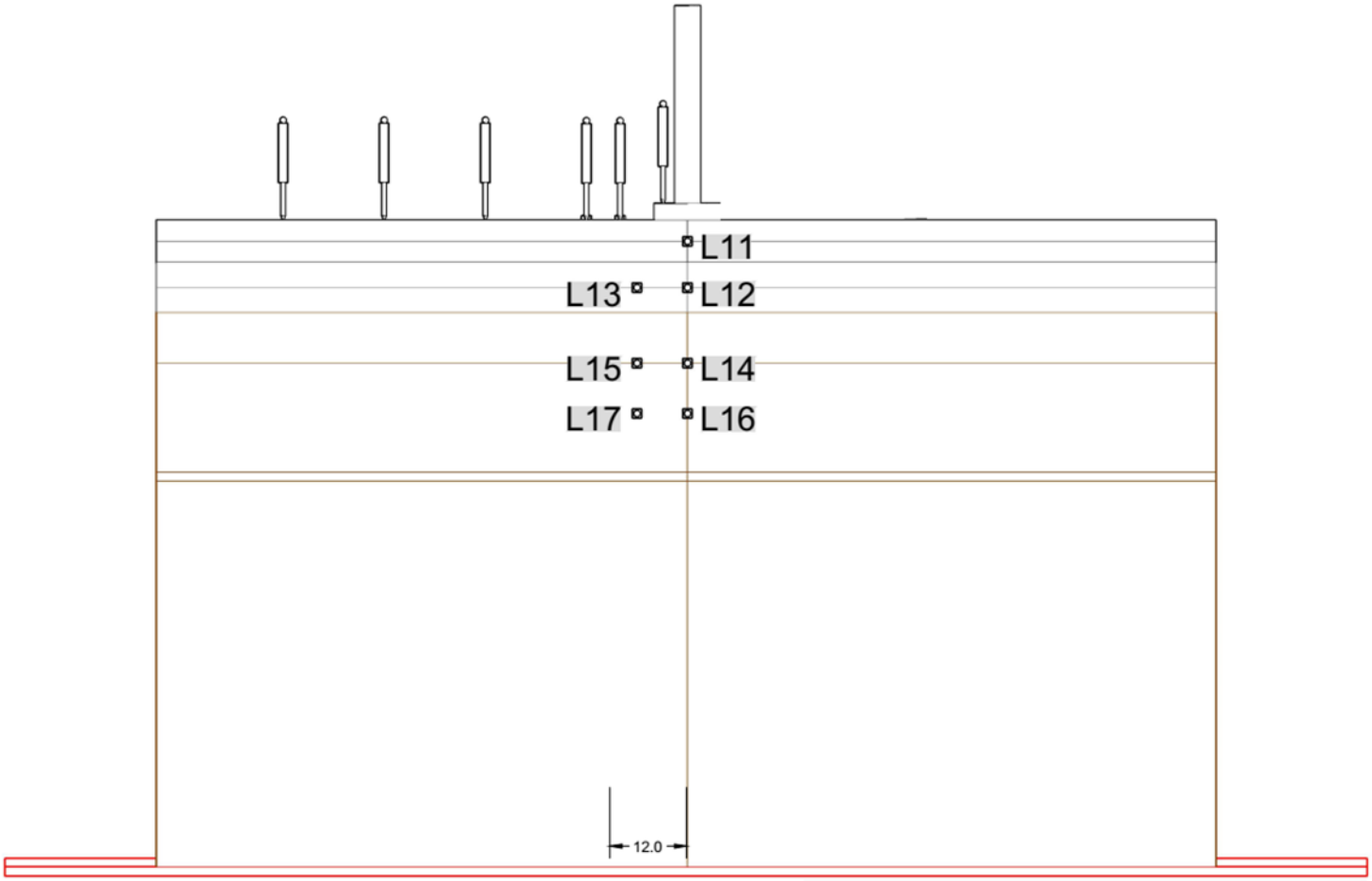



Note: All dimensions are in inches.
L = linear variable differential transformer.

**Figure 20. Illustration. Front elevation of large-scale-box instrumentations in experiment No. 4 (elevation of 77 inches).**

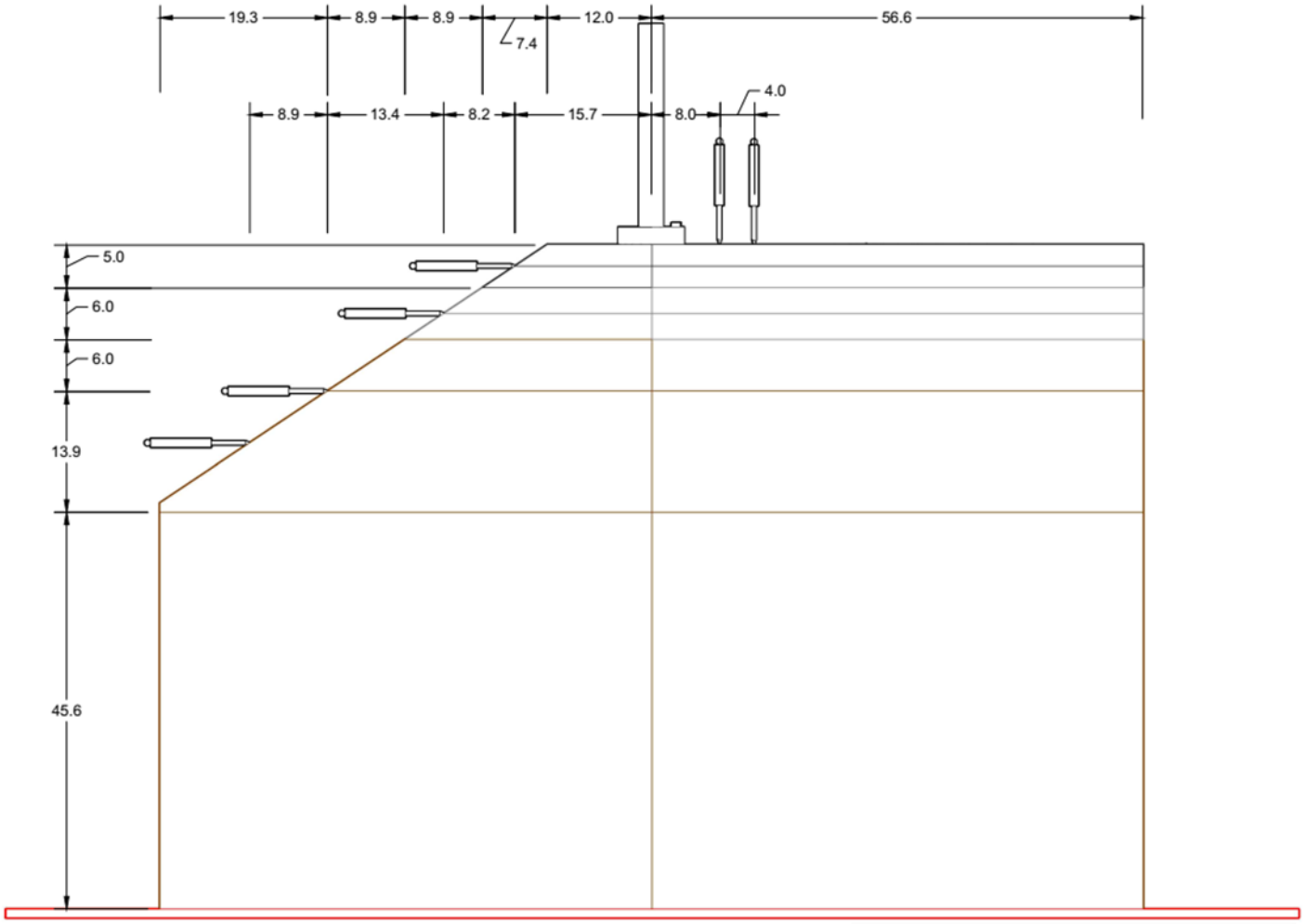



Note: All dimensions are in inches.

**Figure 21. Illustration. Side elevation of large-scale-box instrumentations in experiment No. 4 (elevation of 77 inches).**

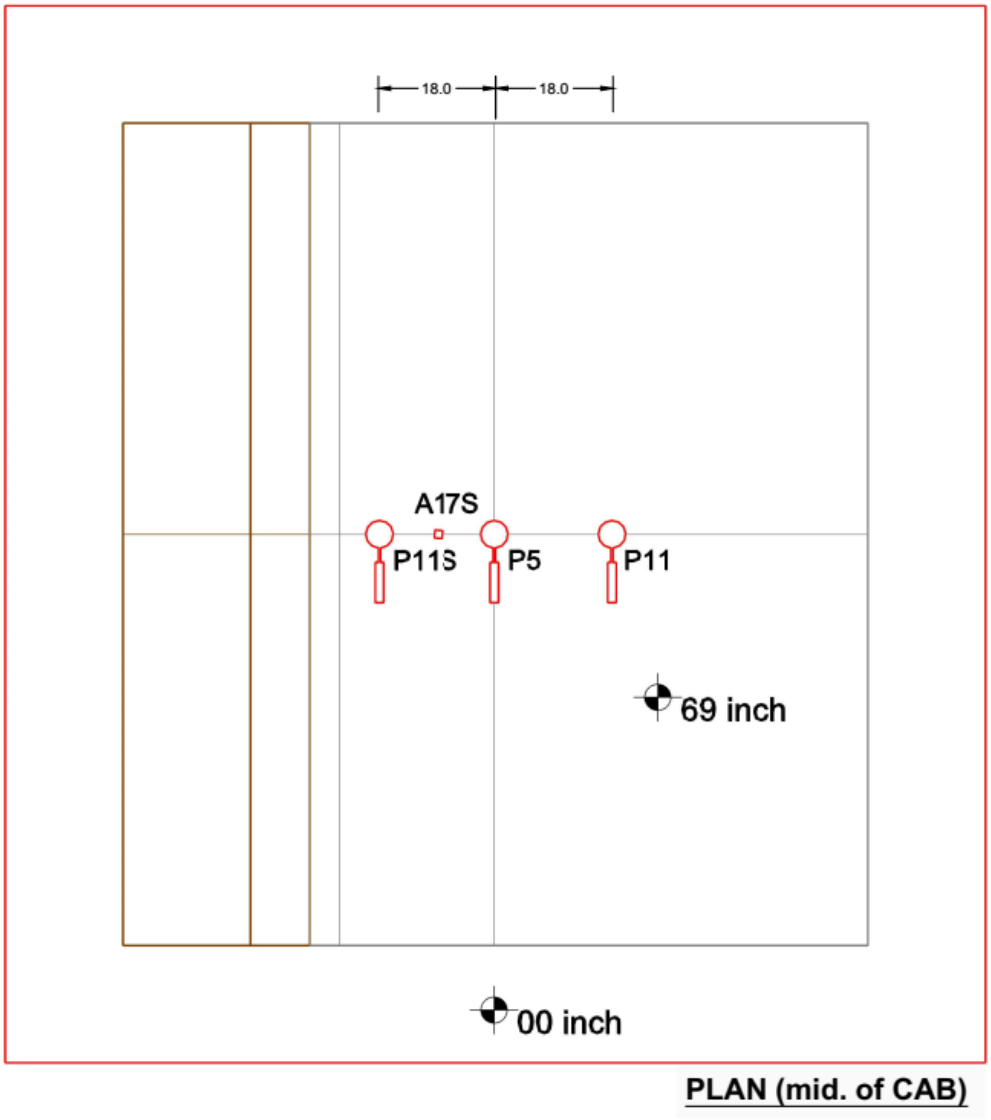



Note: All dimensions are in inches.
P = total earth pressure cell; A = accelerometer.

**Figure 22. Illustration. Plan view of large-scale-box instrumentations in experiment No. 4 (elevation of 69 inches).**

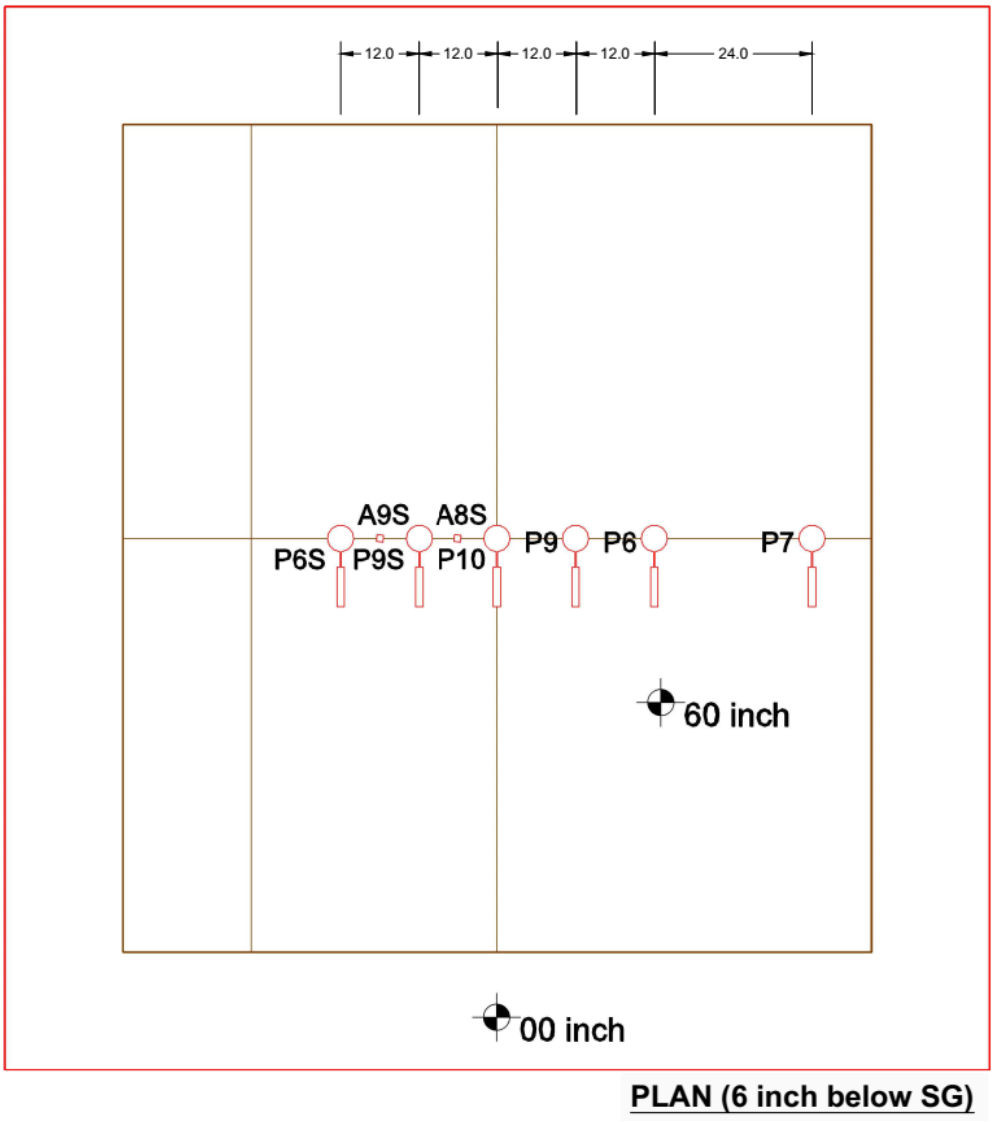



Note: All dimensions are in inches.
P = total earth pressure cell; A = accelerometer.

**Figure 23. Illustration. Plan view of large-scale-box instrumentations in experiment No. 4 (elevation of 60 inches).**

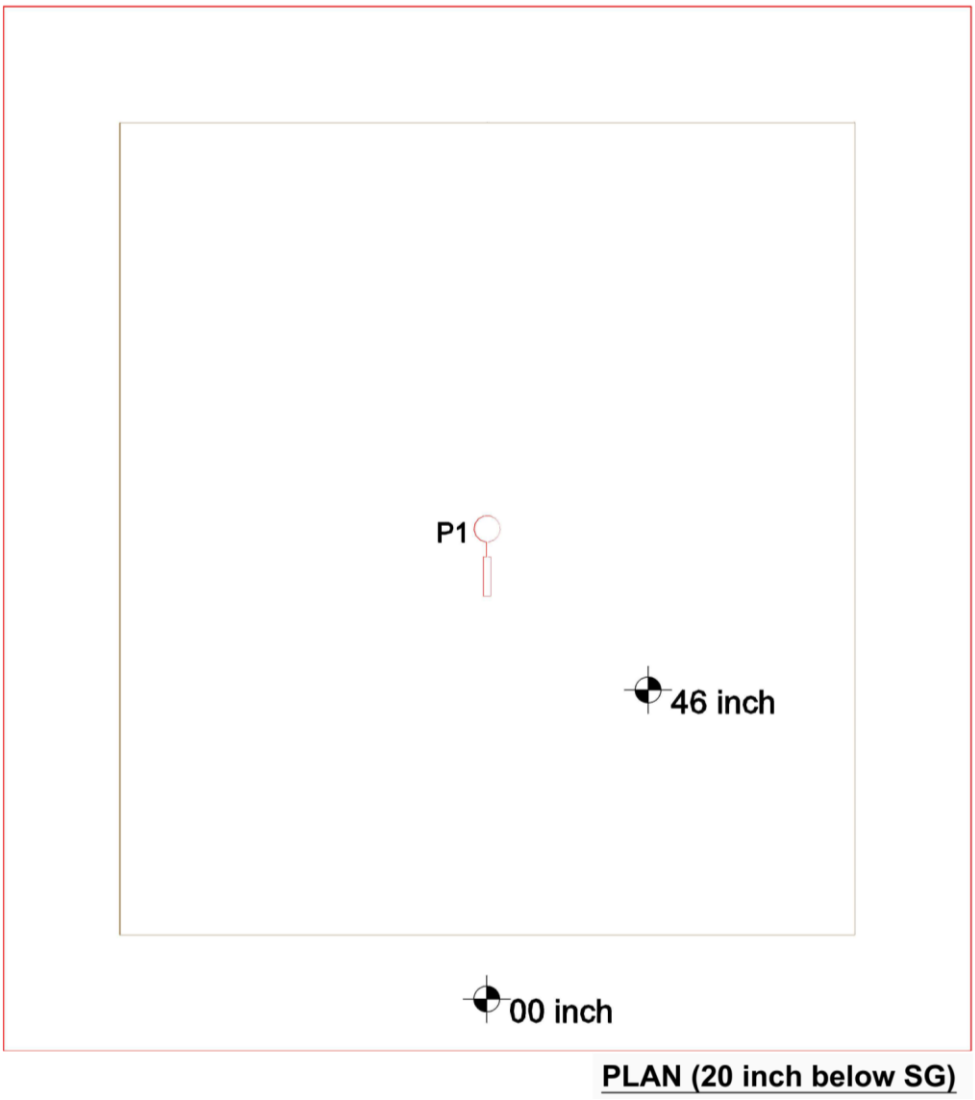



P = total earth pressure cell.

**Figure 24. Illustration. Plan view of large-scale-box instrumentations in experiment No. 4 (elevation of 46 inches).**

## 3.2. COMPARISON OF STRESS MEASUREMENTS

Figure 25 depicts the deflection basins measured in experiment No. 3 and experiment No. 4 at three load levels (i.e., 9,000; 16,000; and 27,000 lb) applied at Loc36. This figure implies that, when the load is far enough from the edge in experiment No. 4, surface deflections are similar to the ones in experiment No. 3, which means that the stiffness properties of the pavement layers in the two experiments are reasonably similar. Consequently, experiment No. 3 can be treated as a control experiment so that any difference in stress measurements at the same location in both experiments can be attributed to the sloped edge.

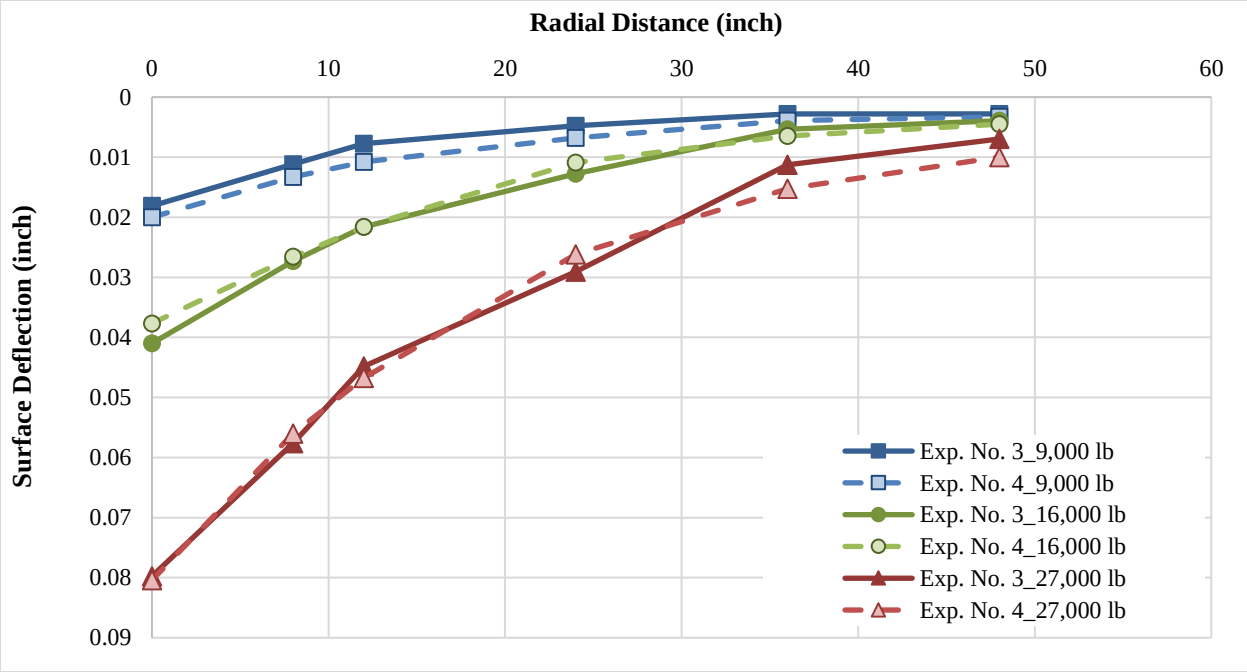




**Figure 25. Graph. Comparison between surface displacements in experiment No. 3 and experiment No. 4 (load applied at Loc36).**

Figure 26 and figure 27 show the measured vertical stresses ($\sigma_v$) in the SG on the nonslope side of the pavement structure with respect to the location of the applied surface load. Compared to the corresponding measured stresses in experiment No. 3, the stress distribution in the nonslope side of the pavement structure was not affected by the sloped edge.

Figure 28 and figure 29 demonstrate the load-induced $\sigma_v$ measured by the total earth pressure cells (TEPCs) that were installed under the exact centerline of the load at different depths in the SG. (In this study, specific TEPCs are denoted by a P and a corresponding number.) These figures show the increase in the measured $\sigma_v$ in experiment No. 4 compared to experiment No. 3.

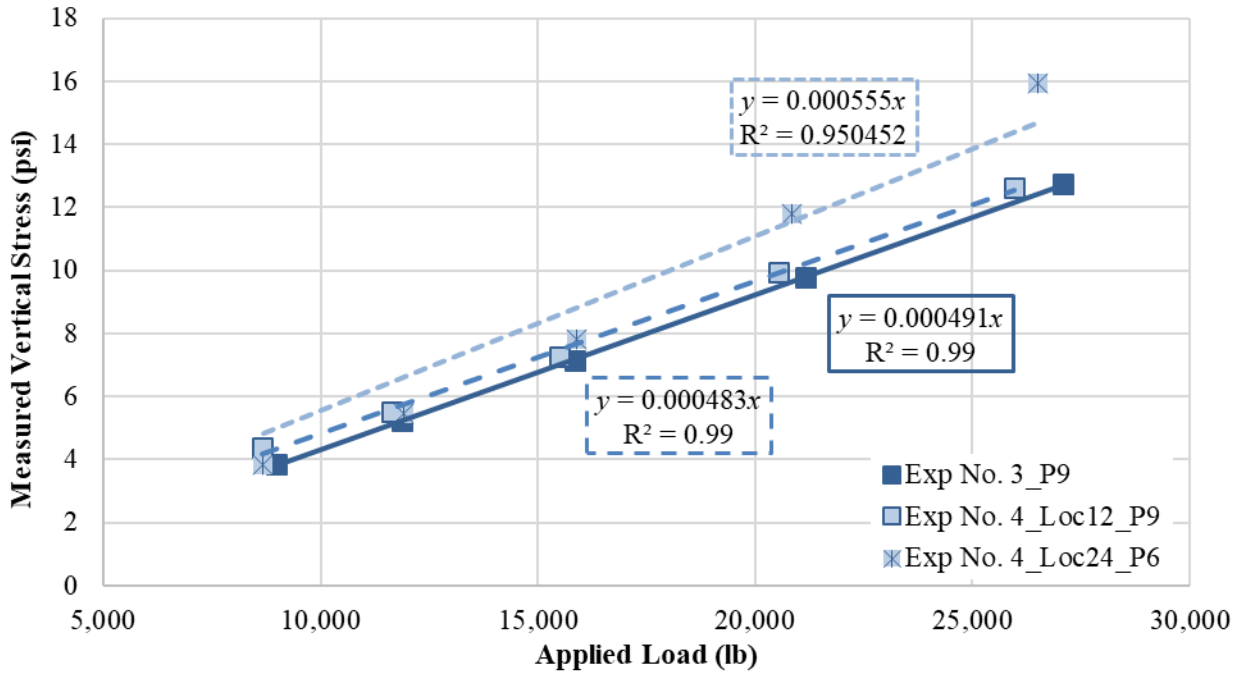




**Figure 26. Graph. Comparison between measured $\sigma_v$ in experiment No. 3 and experiment No. 4 (nonslope side, load applied at Loc12 and Loc24, 6 inches from SG surface, offset from the centerline of the load equal to 12 inches).**

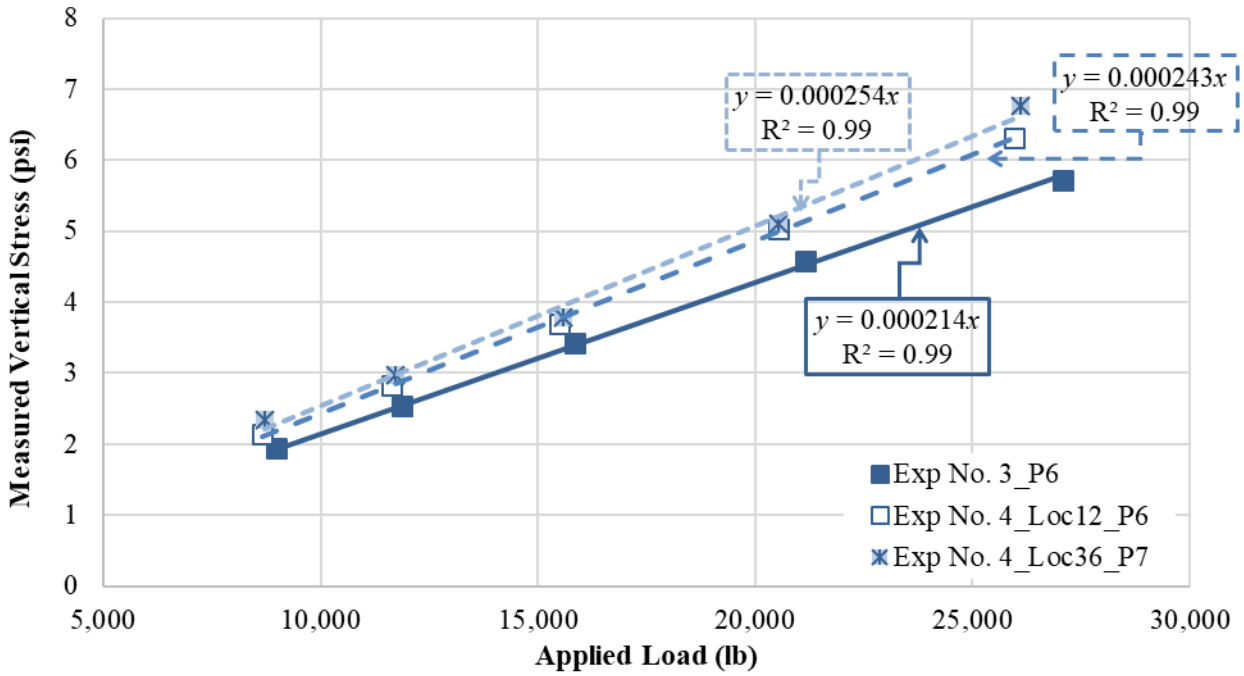




**Figure 27. Graph. Comparison between measured $\sigma_v$ in experiment No. 3 and experiment No. 4 (nonslope side, load applied at Loc12 and Loc36, 6 inches from SG surface, offset from the centerline of the load equal to 24 inches).**

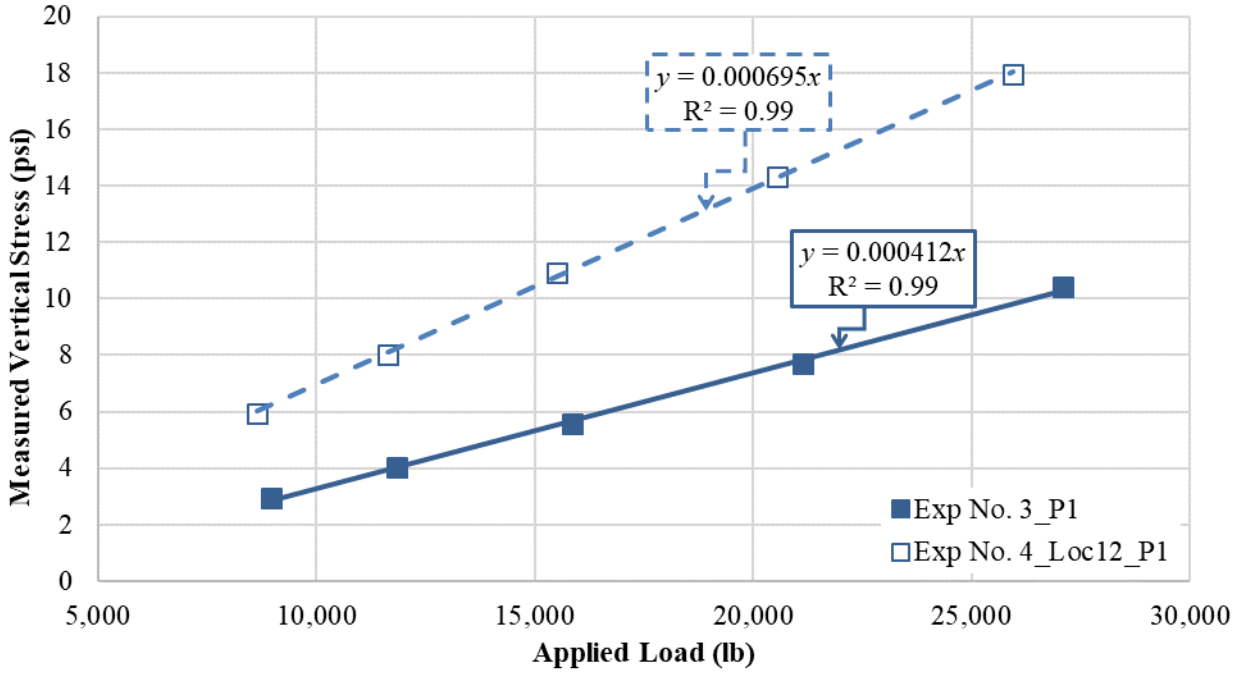




**Figure 28. Graph. Comparison between measured $\sigma_v$ in experiment No. 3 and experiment No. 4 (load applied at Loc12, 20 inches from SG surface, centerline of the load).**

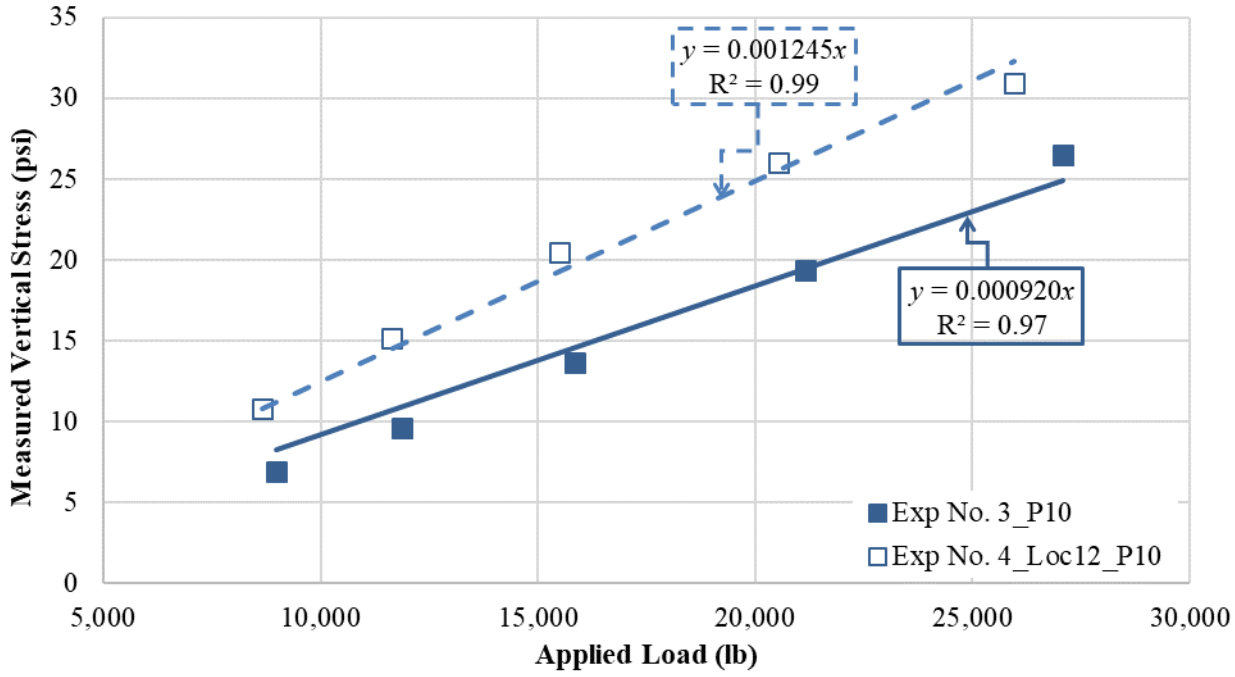




**Figure 29. Graph. Comparison between measured $\sigma_v$ in experiment No. 3 and experiment No. 4 (load applied at Loc12, 6 inches from SG surface, centerline of the load).**

Figure 30 through figure 32 depict the measured $\sigma_v$ at the location of the TEPCs, which were located in the slope side with respect to the applied surface load in experiment No. 4. Figure 30

shows the measured load-induced $\sigma_v$ at 6 inches from the SG surface in experiment No. 4 along with the matching ones in experiment No. 3. For two different distances of surface load from the edge of the slope (i.e., 12 and 24 inches), a significant increase in the measured $\sigma_v$ was observed, which reveals the role the sloped edge had on the stress distribution in the slope side.

Figure 31 and figure 32 represent the stresses measured by P9 and P10 when surface loads were applied at the farthest location from the edge in experiment No. 4 (i.e., Loc36). These figures imply that, although the surface load was applied 36 inches from the edge of the slope, significant change in the $\sigma_v$ distribution, which is attributed to the role of the sloped edge, is expected.

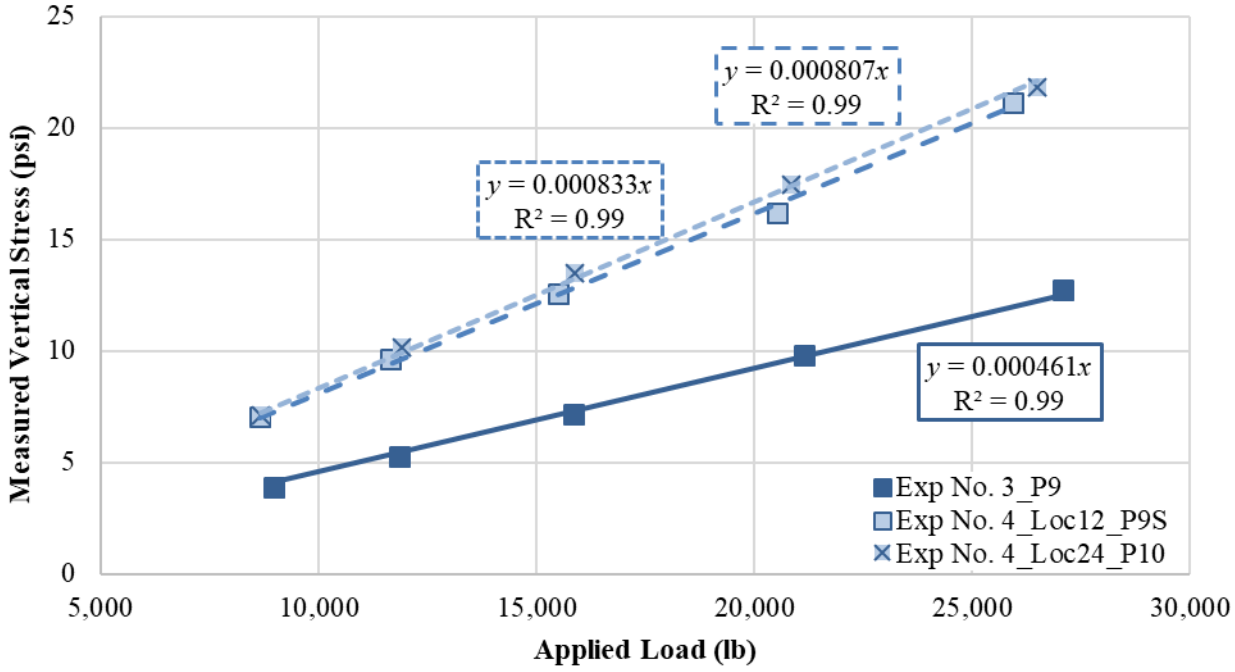




**Figure 30. Graph. Comparison between measured $\sigma_v$ in experiment No. 3 and experiment No. 4 (load applied at Loc12 and Loc24, slope side, 6 inches from SG surface, offset from the centerline of the load equal to 12 inches).**

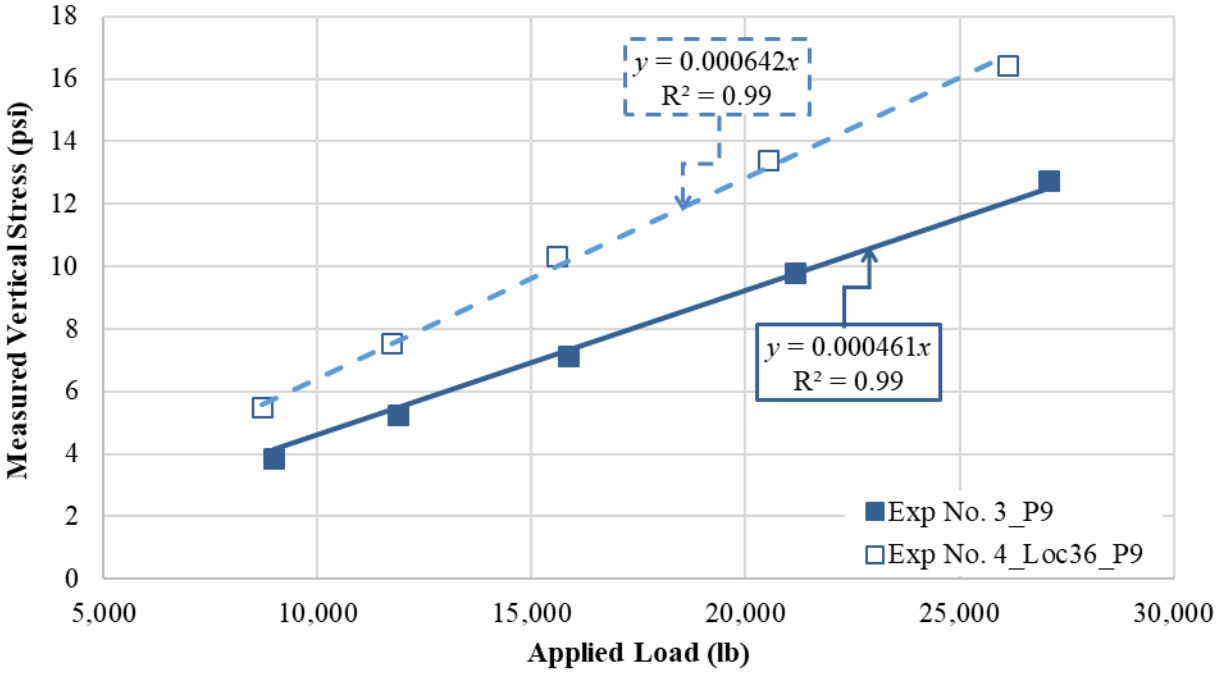




**Figure 31. Graph. Comparison between measured $\sigma_v$ in experiment No. 3 and experiment No. 4 (load applied at Loc36, slope side, 6 inches from SG surface, offset from the centerline of the load equal to 12 inches).**

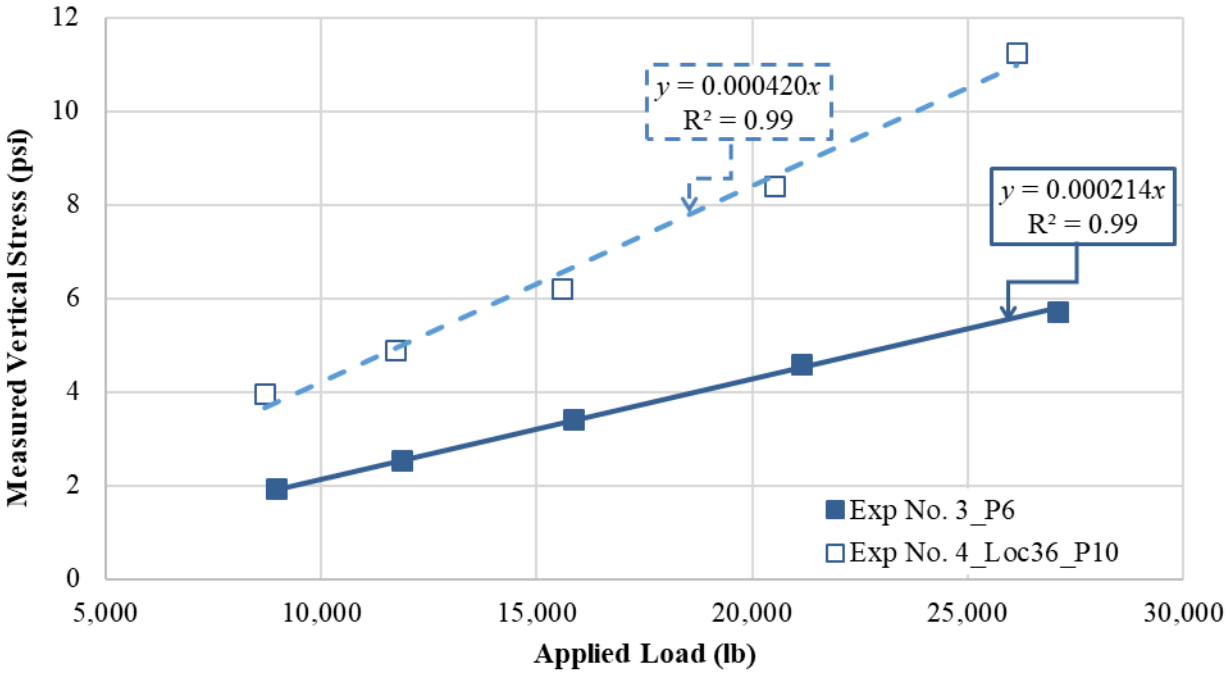




**Figure 32. Graph. Comparison between measured $\sigma_v$ in experiment No. 3 and experiment No. 4 (load applied at Loc36, slope side, 6 inches from SG surface, offset from the centerline of the load equal to 24 inches).**

### 3.3. *SAF*$_{SHOULDER}$

As stated in section 2.1, it is customary in geotechnical practice to double the calculated horizontal stress in the soil medium (i.e., $SAF_{Shoulder}$ equal to 2) when the half-space condition is not present. In order to determine $SAF_{Shoulder}$ for application to stresses computed by 3D-Move Analysis, measured stresses at the location of the TEPCs in experiment No. 4 were compared against the respective calculated stresses from 3D-Move Analysis. Backcalculated moduli for various layers in experiment No. 3 were used in the simulations using 3D-Move Analysis since this experiment was considered the control experiment that represented a pavement structure without a sloped shoulder. The following summarizes the steps involved to determine $SAF_{Shoulder}$.

***Step 1. Use measured surface displacements (deflection basin) in experiment No. 3 to backcalculate the layer moduli at the respective load levels.***

Figure 33 presents the maximum vertical deflections of the pavement surface measurements from the linear variable differential transformer (averaged from five cycles) at each applied load level. The surface-deflection basins at different load levels were employed in the backcalculation analysis using the program BAKFAA.[15] Repeated backcalculation attempts—with many controls intended to minimize the variability of the elastic modulus—revealed that the SG layer should be divided into two sublayers using the Depth to an Apparent Rigid Layer Method.[16]

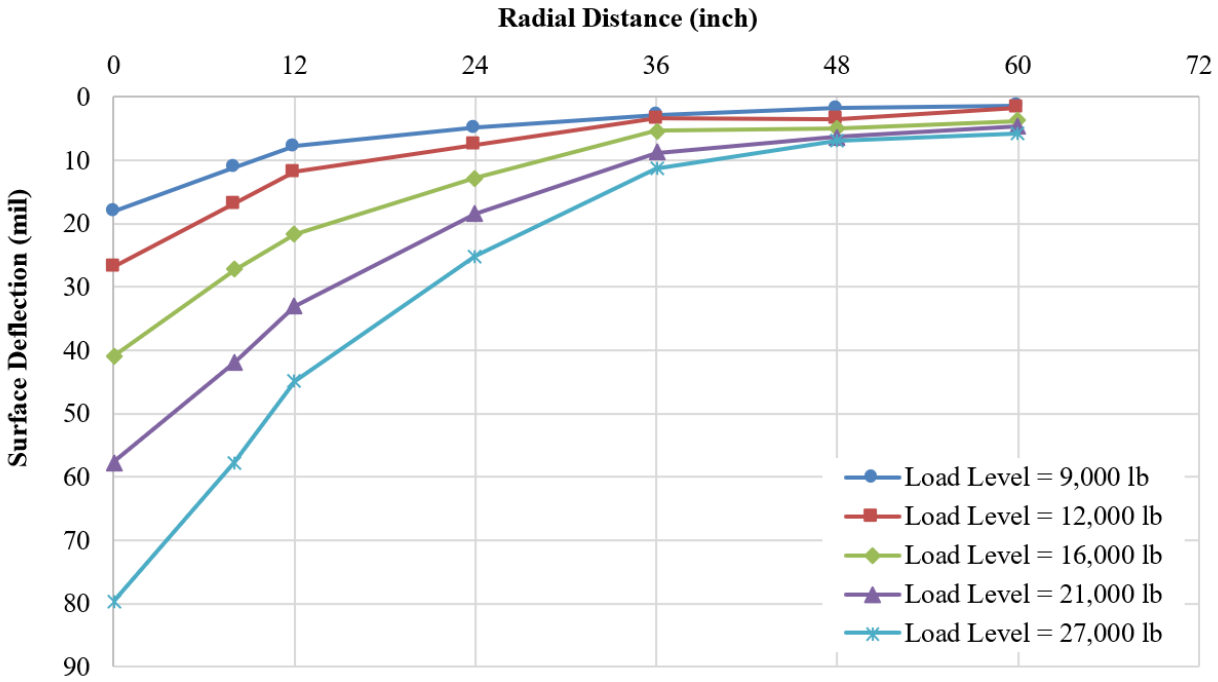



**Figure 33. Graph. Measured deflection basins in experiment No. 3.**

***Step 2. Compare measured $\sigma_v$ at the location of the TEPCs in experiment No.3 with those calculated by 3D-Move Analysis using the associated backcalculated moduli.***

Comparison between the measured and calculated vertical stresses at six different locations in the SG and CAB layers (figure 34) revealed that 3D-Move Analysis is capable of reasonably estimating load-induced stresses when the pavement layers extend laterally to infinity.

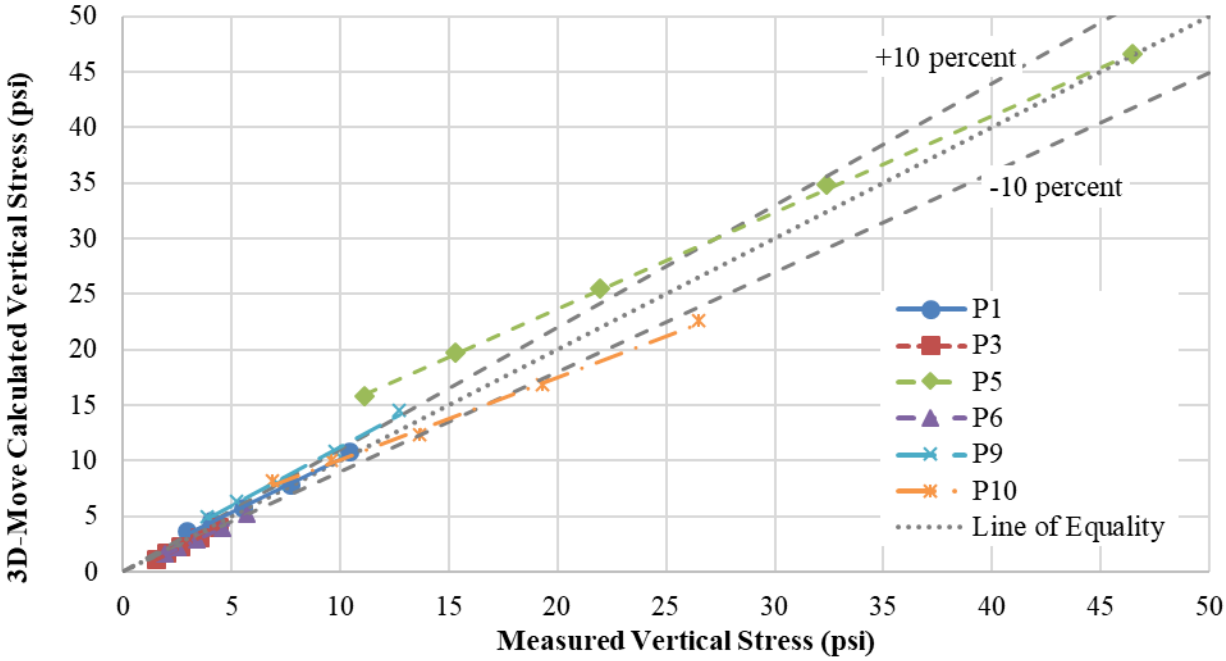




**Figure 34. Graph. Comparison between $\sigma_v$ and $\sigma_v$ calculated using 3D-Move Analysis in experiment No. 3.**

***Step 3: Compute $\sigma_v$ at the location of the TEPCs in experiment No. 4 using 3D-Move Analysis in conjunction with the layer moduli backcalculated from experiment No. 3 and compare with those measured in experiment No. 4.***

As described in section 3.2, measured $\sigma_v$ values on the nonslope side with respect to the applied surface load in experiment No. 4 were similar to the corresponding values recorded in experiment No. 3. Therefore, the comparison between measured $\sigma_v$ in experiment No. 4 and those computed by 3D-Move Analysis were only conducted on data collected from the TEPCs located exactly under the centerline of the load on the slope side with respect to the surface load. The following observations can be made from these comparisons:

- Figure 35 and figure 36 display the comparison between the calculated and measured $\sigma_v$ recorded by P1 and P10 in experiment No. 4, which were located under the centerline of the load (i.e., Loc12) at two different depths. The $\sigma_v$ measured by P1 and P10 are 80 and 40 percent higher than those calculated by 3D-Move, respectively.

- The $\sigma_v$ measured by P1 in experiment No. 4 when the load was applied at Loc24 and Loc36 are presented in figure 37 and figure 38, respectively. These measurements in

comparison to the corresponding ones calculated by 3D-Move Analysis show a 60 percent increase in the load-induced $\sigma_v$ due to the slope.

- Figure 39 depicts the measured load-induced $\sigma_v$ at 6 inches from the SG surface and at a 12-inch radial distance from the centerline of the load in experiment No. 4. when the surface load was applied at two different distances (i.e., 12 and 24 inches) from the edge of the slope. This figure shows an almost 60-percent increase in the measured $\sigma_v$ compared to $\sigma_v$ calculated by 3D-Move Analysis at the same locations.

- As shown in figure 40, at the 24-inch offset from the centerline of the surface load when applied 36 inches from the edge (Loc36), the measured $\sigma_v$ were 80-percent higher than those calculated by 3D-Move Analysis.

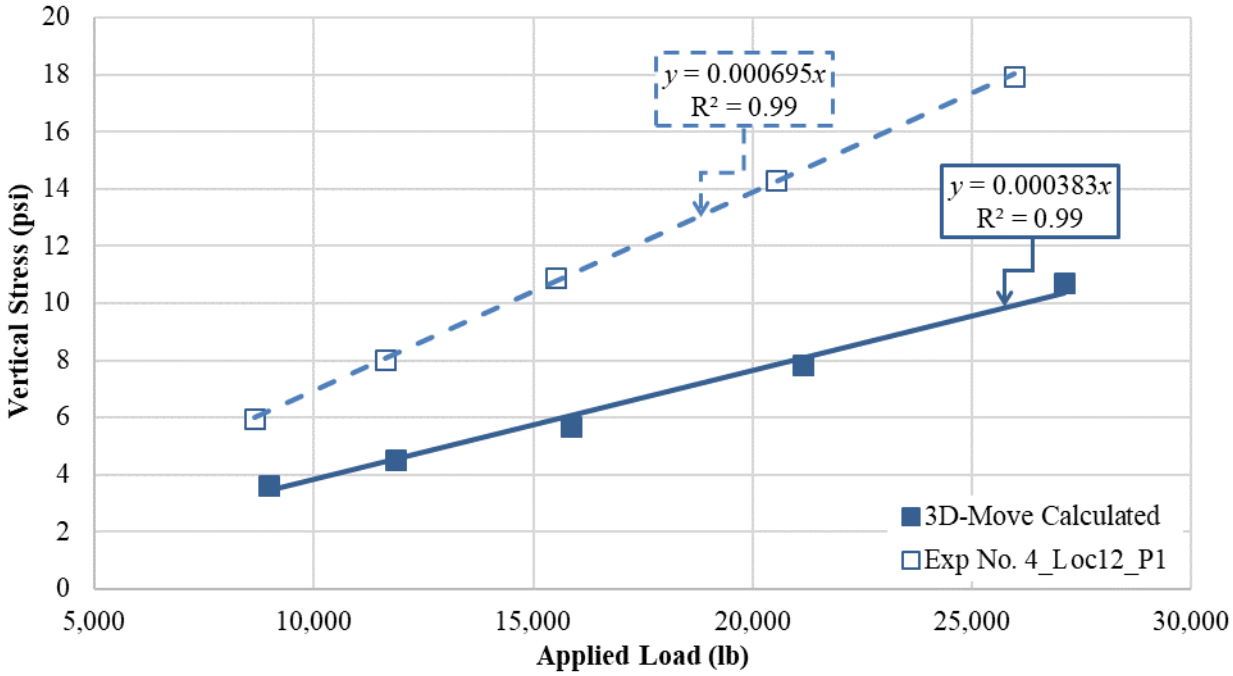




**Figure 35. Graph. Comparison between $\sigma_v$ and $\sigma_v$ calculated using 3D-Move Analysis in experiment No. 4 (20 inches from SG surface, centerline of the load).**

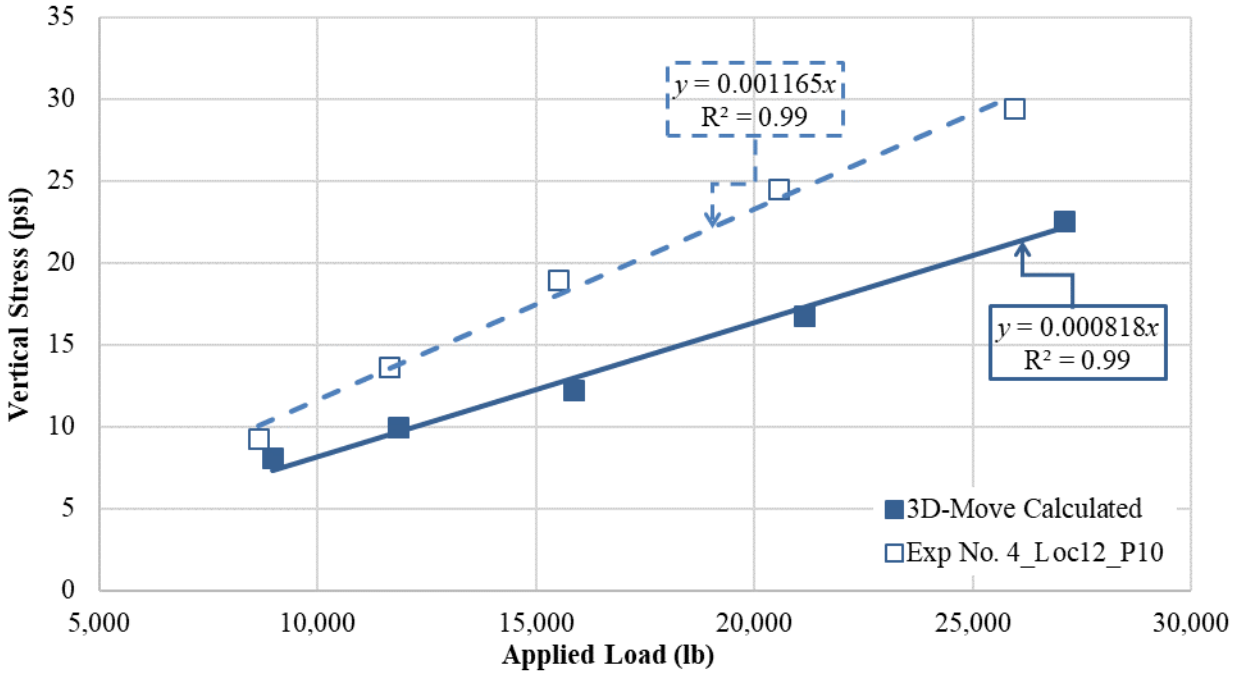




**Figure 36. Graph. Comparison between $\sigma_v$ and $\sigma_v$ calculated using 3D-Move Analysis in experiment No. 4 (6 inches from SG surface, centerline of the load).**

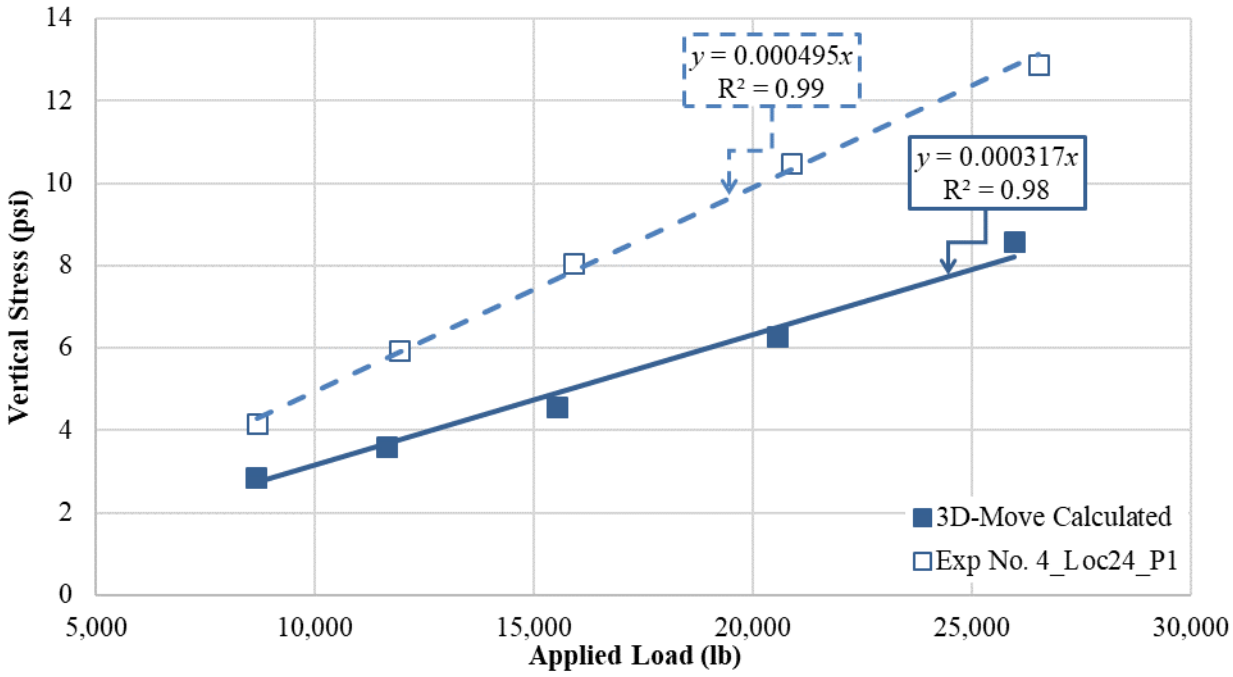




**Figure 37. Graph. Comparison between $\sigma_v$ and $\sigma_v$ calculated using 3D-Move Analysis in experiment No. 4 (slope side, 20 inches from SG surface, offset from the centerline of the load equal to 12 inches).**

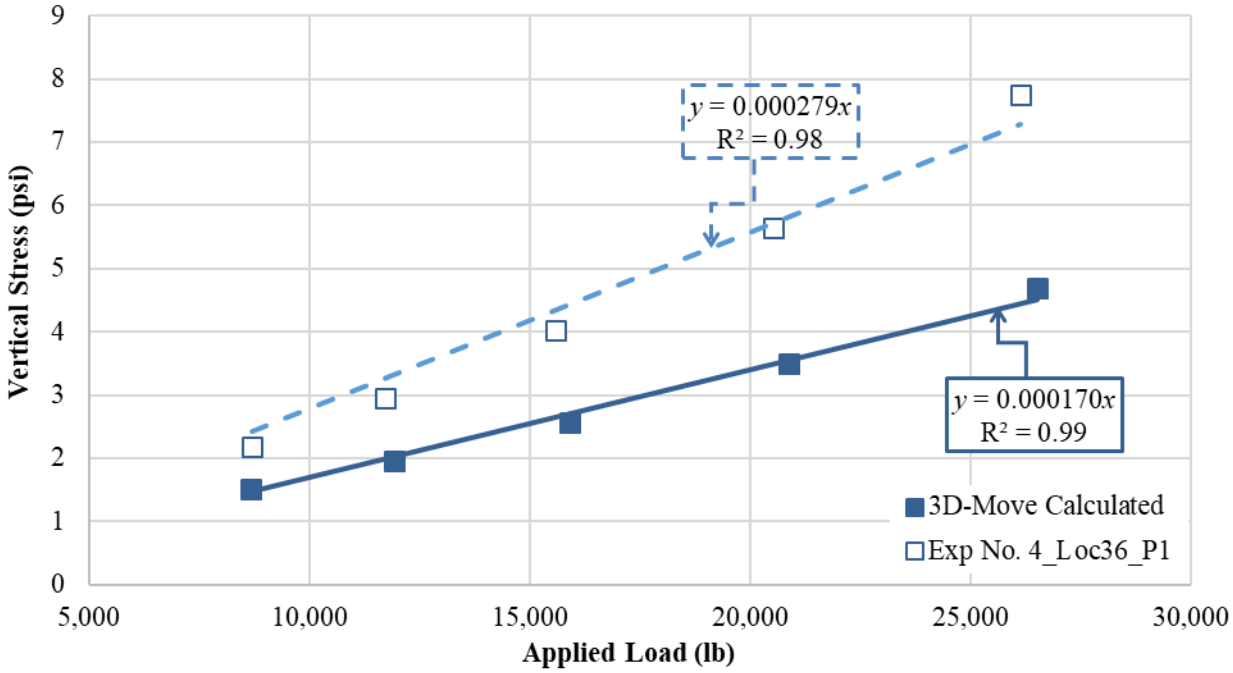




**Figure 38. Graph. Comparison between $\sigma_v$ and $\sigma_v$ calculated using 3D-Move Analysis in experiment No. 4 (slope side, 20 inches from SG surface, offset from the centerline of the load equal to 24 inches).**

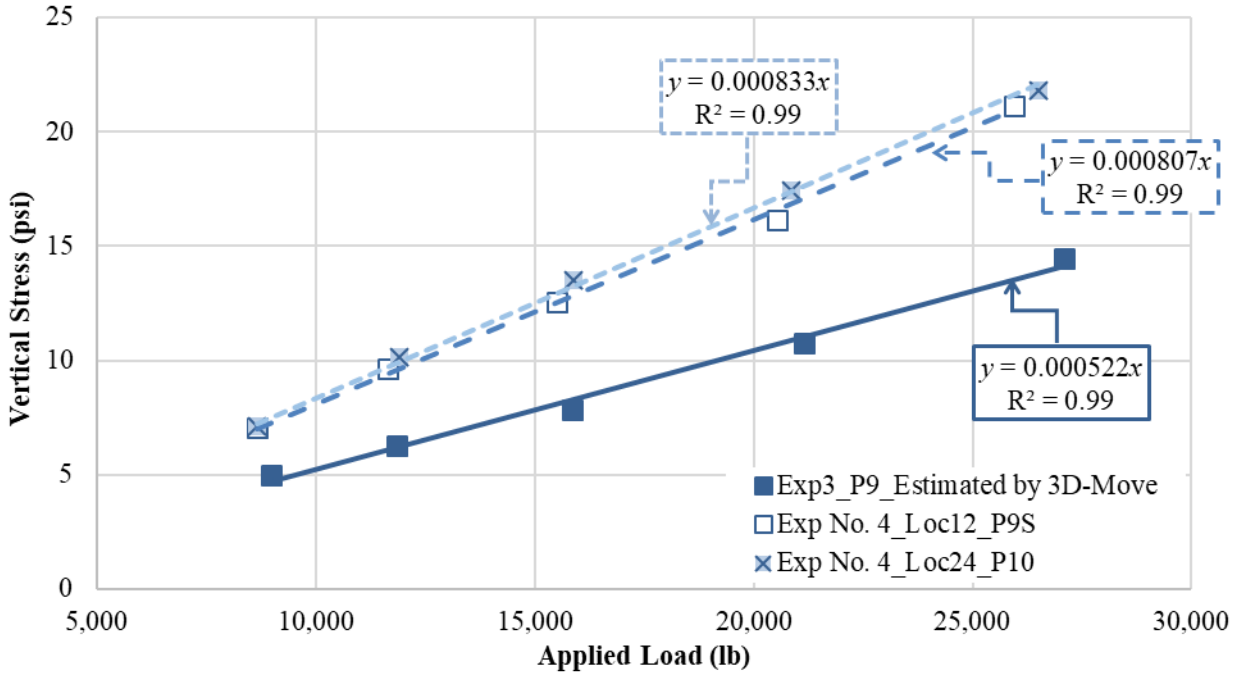




**Figure 39. Graph. Comparison between $\sigma_v$ and $\sigma_v$ calculated using 3D-Move Analysis in experiment No. 4 (slope side, 6 inches from SG surface, offset from the centerline of the load equal to 12 inches).**

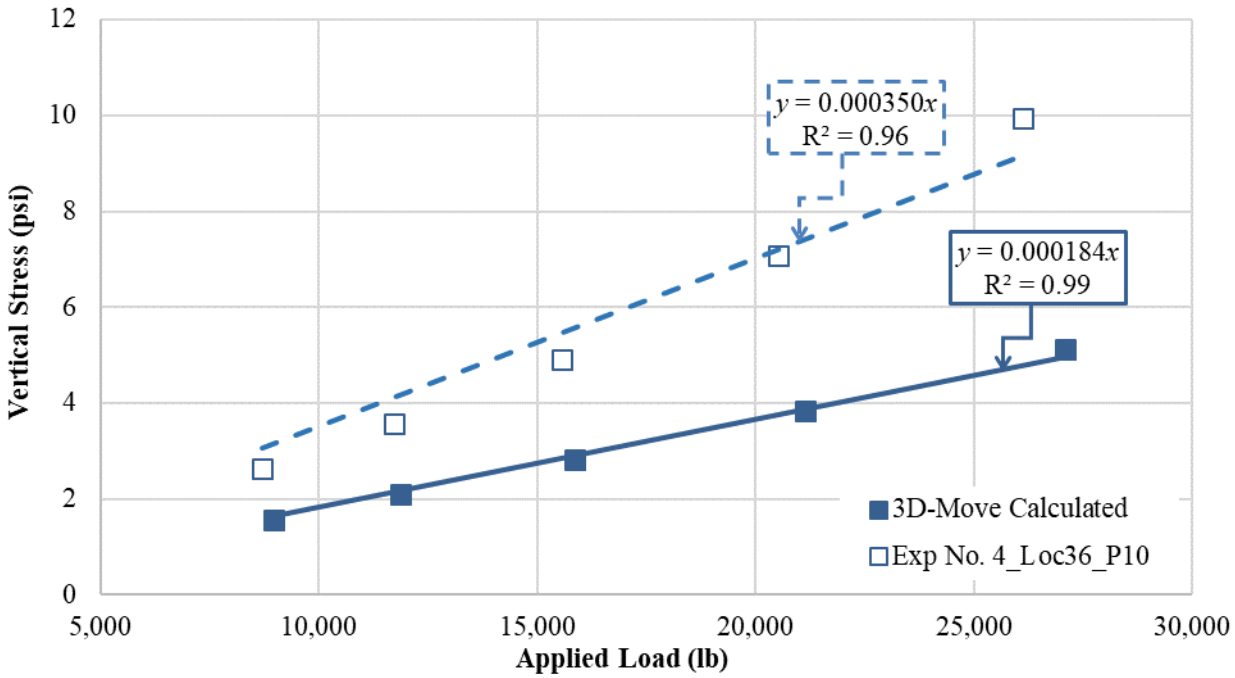




**Figure 40. Graph. Comparison between $\sigma_v$ and $\sigma_v$ calculated using 3D-Move Analysis in experiment No. 4 (slope side, 6 inches from SG surface, offset from the centerline of the load equal to 24 inches).**

Using the data presented in figure 35 through figure 40, $SAF_{Shoulder}$ was computed, and the results are presented in table 2. It can be concluded that sloped shoulders play a major role in stress distribution within a pavement structure, particularly in the slope side. $SAF_{Shoulder}$ ranged from 1.4 to 1.8, with an average of 1.63. Accordingly, $SAF_{Shoulder}$ equal to 1.6 should be used to adjust the calculated stresses using 3D-Move Analysis in the presence of a sloped shoulder.

This conclusion was derived from observations based on experiment No. 3 and experiment No. 4. However, the influence of different parameters—such as pavement structure and layer thicknesses, angle of the slope, distance of the surface load from the edge of the slope, distance of response points from the slope and surface load, etc.—requires further investigation by conducting complementary experiments and additional numerical analyses, which is recommended for future studies.

**Table 2. Summary of computed $SAF_{Shoulder}$.**

| TEPC | Depth | Location of Surface Load in Experiment No. 4 | Offset From Centerline of Load | $SAF_{Shoulder}$ |
|---|---|---|---|---|
| P1 | 20 inches from SG surface | Loc12 | 0 inch | 1.4 |
| P10 | 6 inches from SG surface | Loc12 | 0 inch | 1.8 |
| P1 | 20 inches from SG surface | Loc24 | 12 inches | 1.6 |
| P1 | 20 inches from SG surface | Loc36 | 24 inches | 1.6 |
| P9S* | 6 inches from SG surface | Loc12 | 12 inches | 1.6 |
| P10 | 6 inches from SG surface | Loc24 | 12 inches | 1.6 |
| P10 | 6 inches from SG surface | Loc36 | 24 inches | 1.8 |

*S denotes TEPC on the slope side.

# CHAPTER 4. VALIDATION OF SLOPE-STABILITY WEDGE METHOD FOR SHL-VEHICLE MOVEMENTS

Investigating the applicability of the proposed approach to evaluate the stability of a sloped, layered medium consisting of typical pavement-layer configurations and properties is a concern because slope-stability failure methods have traditionally been used for homogenous or layered soil mediums. In this chapter the exercise to evaluate the validity of the proposed wedge method using experiment No. 4 is presented.

## 4.1. *FOS* FOR A SLOPED EDGE IN EXPERIMENT NO. 4

To evaluate the applicability of the wedge method to measure slope stability, *FOS* for the sloped edge in experiment No. 4 was determined when the FWD loads were applied at three locations (i.e., Loc12, Loc24, and Loc36). (The pavement structure, instrumentation plan, and loading protocol can be found in section 3.1.) Figure 41 is an illustration of the pavement structure and loading locations in experiment No. 4. In this figure, different failure wedges with horizontal and inclined slip surfaces were considered. A spacing between the horizontal slip surfaces of 3 inches was selected.

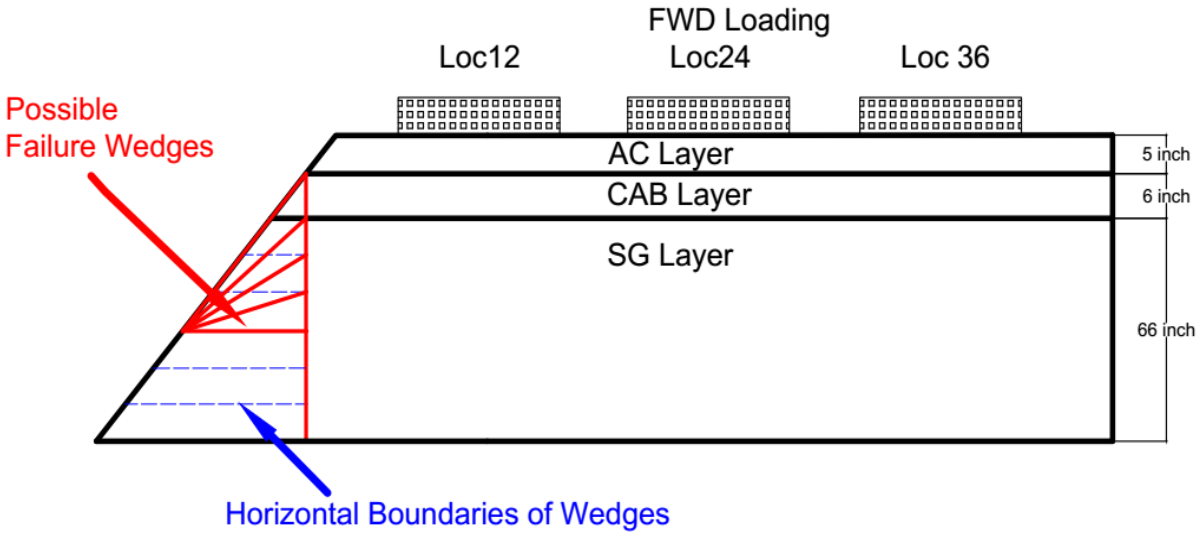




**Figure 41. Illustration. Schematic of experiment No. 4.**

As stated in chapter 2, the wedge method assumes the plane strain condition for the slope-stability analysis under an SHL-vehicle movement because the length of SHL vehicles can be substantial. However, in experiment No. 4, the FWD load was applied on an 11.9-inch circular plate, meaning that the plane strain assumptions do not hold true. Therefore, a three-dimensional (3D) analysis of the wedge method should be used.

Figure 42 illustrates the possible 3D failure wedge in experiment No. 4 where the width of the wedge ($B_{wedge}$) equal to 11.9 inches (i.e., the width of the FWD plate) was assumed. A diagram of the force applied on the failure wedge is shown in figure 43. A total of seven forces acted on

the failure wedge. Five of these forces, $W$, $T_D$, $F_D$, $Q$, and $P$ (due to the FWD load), are defined in section 2.1. The following are two additional forces:

- Developed resisting $c$ force resulting from the mobilized $c$ acting on the side surfaces (i.e., front and back) ($T'_D$).
- The resistive force from the side soil that makes an angle ($\phi_D$) with the normal to the side surfaces (i.e., front and back) ($P_D$).

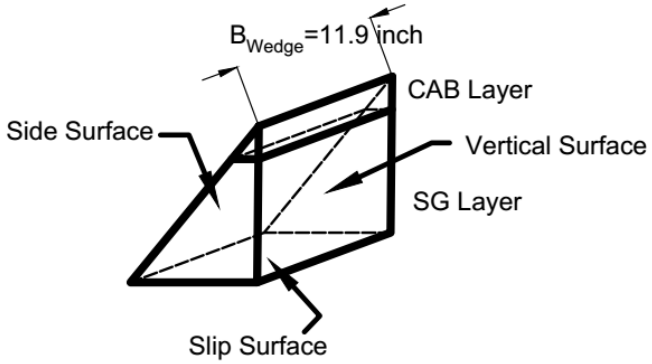




**Figure 42. Illustration. Possible failure wedge.**

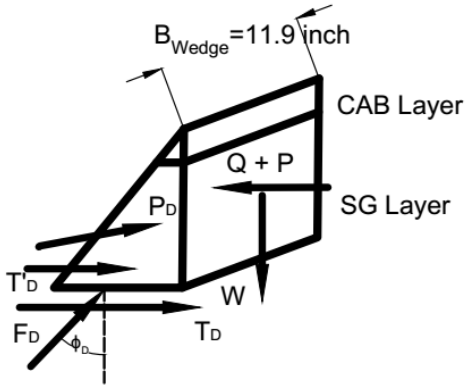




**Figure 43. Illustration. Diagram of the force applied on the possible failure wedge.**

As shown in section 2.1, the Rankine active earth pressure was used to determine the $Q$. The horizontal stress distribution on the vertical side of the failure wedge was computed with 3D-Move Analysis using the backcalculated resilient moduli and was subsequently adjusted with $SAF_{shoulder}$ equal to 1.6. $T'_D$ was only applied on the trapezoidal side surfaces composed of SG ($A_{SG}$) because cohesionless properties for the base material were assumed.

Meyerhoff et al. proposed that $P_D$ is a passive resistance force from the surrounding SG and can be determined using the Rankine passive earth pressure ($\sigma_P$) expressed by the equations in

figure 44 and figure 45.[17] $\sigma_0$ should be calculated at the center of gravity of the triangular area of the base layer and the trapezoidal area of the SG layer within the failure surface.

$$K_p = \tan^2\left(45 + \frac{\phi}{2}\right)$$

**Figure 44. Equation. Calculation of $K_p$.**

$$\sigma_P = 2\left(\sigma_0 K_p + 2c\sqrt{K_p}\right)$$

**Figure 45. Equation. Calculation of $\sigma_P$.**

Using the force equilibrium equations in parallel and perpendicular directions to the slip surface, *FOS* can be determined, which is expressed in figure 46. There is no explicit solution for the calculation of *FOS*.

$$\frac{W\tan\phi}{FOS} + \frac{clB_{wedge}}{FOS} + \frac{2cA_{SG}}{FOS} + P_D \sin\left(\tan^{-1}\left(\frac{\tan\phi}{FOS}\right)\right) = P + Q$$

**Figure 46. Equation. *FOS* against failure for the wedges in experiment No. 4.**

As a representative example of calculations, *FOS* for the possible failure wedge where the horizontal slip surface was located 9 inches from the SG surface (i.e., 20 inches from the pavement surface) equal to 3.5 was calculated. In this exercise, the FWD loading at the highest load level (about 27,000 lb) applied at Loc12 was considered. Table 3 summarizes the properties of the materials used in experiment No. 4. Figure 47 depicts the calculated horizontal stresses adjusted by $SAF_{shoulder}$ equal to 1.6 using 3D-Move Analysis.

For the same load level and location (i.e., about 27,000 lb at Loc12), a minimum *FOS* equal to 1.3 was determined for the possible failure wedge where the horizontal slip surface is located 3 inches from the SG surface (i.e., 14 inches from the pavement surface). For a similar load level applied at Loc24 and Loc36, minimum *FOS* values equal to 1.6 and 3.1 were determined, respectively. Slope failure was not observed for the same loading cases in experiment No. 4, confirming that the proposed wedge method is capable of analyzing the stability of a sloped, layered medium consisting of typical pavement-layer configurations and properties.

**Table 3. Properties of materials in experiment No. 4.**

| Properties | Value |
|---|---|
| Density of CAB material | 125 pcf |
| $\phi$ of CAB material | 38 degrees |
| Density of SG material | 110 pcf |
| $\phi$ of SG material | 38 degrees |
| *c* of SG material | 2 psi |

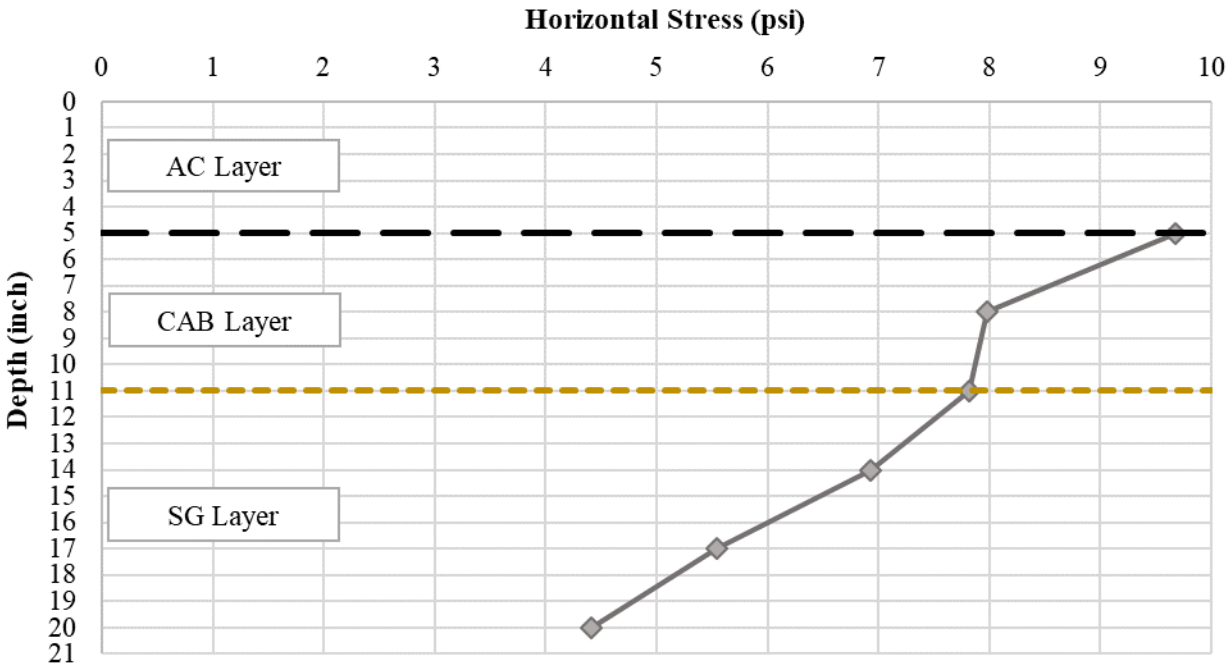



**Figure 47. Graph. Adjusted horizontal stresses calculated using 3D-Move Analysis.**

# CHAPTER 5. SUMMARY AND CONCLUSION

Although it is recommended that an SHL vehicle stay away from a pavement edge to avoid sloped pavement shoulder failure, doing so is not always possible when an SHL vehicle is traveling along a narrow roadway. Therefore, in such cases of SHL-vehicle movements, slope-stability analysis is necessary.

In this study, the wedge method, which is a well-accepted slope stability–analysis methodology in geotechnical practice, was modified so that the stability of a sloped, layered medium consisting of pavement layers with distinct properties could be evaluated under SHL-vehicle movements. This method evaluates the stability of possible failure wedges by considering them as a rigid sliding mass or gravity-retaining structure. *P* (i.e., the SHL vehicle) is the major component of the horizontal driving force leading to the instability of a failure wedge. 3D-Move Analysis was used to compute the horizontal stresses since it accounts for the viscoelastic properties of the AC layer as well as the moving load with nonuniform tire–pavement interface stresses on a loaded area of any shape.

The computed stresses using 3D-Move Analysis need to be modified to account for the role of the sloped shoulder near the edge of the pavement because this software assumes that pavement layers extend laterally to infinity. To this end, $SAF_{Shoulder}$ was determined based on the results obtained from two large-scale experiments, experiment No. 3 and experiment No. 4. Both experiments had similar pavement structures, except experiment No. 4 had a sloped edge. The measured stresses at the location of the TEPCs in experiment No. 4 were compared against the respective calculated stresses from 3D-Move Analysis. In these calculations, backcalculated moduli for the various layers from experiment No. 3 (i.e., the control experiment) were used.

The sloped shoulder was found to play a major role in the stress distribution within a pavement structure, particularly in the slope side. Accordingly, in the presence of sloped shoulder, it is recommended to have $SAF_{Shoulder}$ equal to 1.6 to adjust the calculated stresses from 3D-Move Analysis. The validity of the proposed wedge method using experiment No. 4 was verified.

Further investigation by conducting complementary experiments and additional numerical analyses is recommended. Such analyses should consider various scenarios of flexible pavement structures, slope angles, distance of the surface load from the edge of the slope, etc., to cover other cases that were not considered as part of this study in the determination of $SAF_{Shoulder}$.

## REFERENCES


1. Hajj, E.Y., Siddharthan, R.V., Nabizadeh, H., Elfass, S., Nimeri, M., Kazemi, S.F., Batioja-Alvrez, D.D., and Piratheepan, M. (2018). *Analysis Procedures for Evaluating Superheavy Load Movement on Flexible Pavements, Volume I: Final Report*, Report No. FHWA-HRT-18-049, Federal Highway Administration, Washington, DC.

2. Nimeri, M., Nabizadeh, H., Hajj, E.Y., Siddharthan, R.V., Elfass, S, and Piratheepan, M. (2018). *Analysis Procedures for Evaluating Superheavy Load Movement on Flexible Pavements, Volume II: Appendix A, Experimental Program*, Report No. FHWA-HRT-18-050, Federal Highway Administration, Washington, DC.

3. Nimeri, M., Nabizadeh, H., Hajj, E.Y., Siddharthan, R.V., and Elfass, S. (2018). *Analysis Procedures for Evaluating Superheavy Load Movement on Flexible Pavements, Volume III: Appendix B, Superheavy Load Configurations and Nucleus of Analysis Vehicle*, Report No. FHWA-HRT-18-051, Federal Highway Administration, Washington, DC.

4. Nabizadeh, H., Hajj, E.Y., Siddharthan, R.V., and Elfass, S. (2018). *Analysis Procedures for Evaluating Superheavy Load Movement on Flexible Pavements, Volume IV: Appendix C, Material Characterization for Superheavy Load Movement Analysis*, Report No. FHWA-HRT-18-052, Federal Highway Administration, Washington, DC.

5. Nabizadeh, H., Hajj, E.Y., Siddharthan, R.V., Nimeri, M., Elfass, S., and Piratheepan, M. (2018). *Analysis Procedures for Evaluating Superheavy Load Movement on Flexible Pavements, Volume V: Appendix D, Estimation of Subgrade Shear Strength Parameters Using Falling Weigh Deflectometer*, FHWA-HRT-18-053, Federal Highway Administration, Washington, DC.

6. Nabizadeh, H., Nimeri, M., Hajj, E.Y., Siddharthan, R.V., Elfass, S., and Piratheepan, M. (2018). *Analysis Procedures for Evaluating Superheavy Load Movement on Flexible Pavements, Volume VI: Appendix E, Ultimate and Service Limit Analyses*, Report No. FHWA-HRT-18-054, Federal Highway Administration, Washington, DC.

7. Nabizadeh, H., Elfass, S., Hajj, E.Y., Siddharthan, R.V., Nimeri, M., and Piratheepan, M. (2018). *Analysis Procedures for Evaluating Superheavy Load Movement on Flexible Pavements, Volume VIII: Appendix G, Risk Analysis of Buried Utilities Under Superheavy Load Vehicle Movements*, Report No. FHWA-HRT-18-056, Federal Highway Administration, Washington, DC.

8. Batioja-Alvarez, D.D., Hajj, E.Y., and Siddharthan, R.V. (2018). *Analysis Procedures for Evaluating Superheavy Load Movement on Flexible Pavements, Volume IX: Appendix H, Analysis of Cost Allocation Associated with Pavement Damage Under a Superheavy Load Vehicle Movement*, Report No. FHWA-HRT-18-057, Federal Highway Administration, Washington, DC.

9. Kazemi, S.F., Nabizadeh, H., Nimeri, M., Batioja-Alvarez, D.D., Hajj, E.Y., Siddharthan, R.V., and Hand, A.J.T. (2018). *Analysis Procedures for Evaluating Superheavy Load Movement on Flexible Pavements, Volume X: Appendix I, Analysis Package for Superheavy Load Vehicle Movement on Flexible Pavement (SuperPACK)*, Report No. FHWA-HRT-18-058, Federal Highway Administration, Washington, DC.

10. 3D-Move Analysis software V2.1. (2013). University of Nevada, Reno, NV. Available online at: http://www.arc.unr.edu/Software.html#3DMove, last accessed September 19, 2017.

11. Fernando, E.G. (1997). *Guidelines for Evaluating Superheavy Load Routes*, Report No. TX-98/3923-S, Texas Transportation Institute, College Station, TX.

12. U.S. Army Corps of Engineers. (2003). *Slope Stability*, Department of the Army, Washington, DC.

13. Southern California Earthquake Center. (2002). *Recommended Procedures for Implementation of DMG Special Publication 117 Guidelines for Analyzing and Mitigating Landslide Hazards in California.* SCEC, Los Angeles, CA. Available online: http://scecinfo.usc.edu/resources/catalog/LandslideProceduresJune02.pdf, last accessed February 21, 2019.

14. Das, B.M. and Sobhan, K. (2014). *Principles of Geotechnical Engineering*, Cengage Learning, Stamford, CT.

15. BAKFAA software V2.0. (2012). Federal Aviation Administration, Washington, DC.

16. Rohde, G.T. and Scullion, T. (1990). *MODULUS 4.0: Expansion and Validation of the MODULUS Backcalculation System*, Report No. FHWA/TX-91/1123-3, Texas Transportation Institute, College Station, TX.

17. Meyerhof, G.G. and Hanna, A.M. (1978). "Ultimate Bearing Capacity of Foundations on Layered Soil under Inclined Load." *Canadian Geotechnical Journal*, *15*(4), pp. 565–572, NRC Research Press, Ottawa, Canada.

HRDI-20/03-19(WEB)E